

This is an Open Access document downloaded from ORCA, Cardiff University's institutional repository: <https://orca.cardiff.ac.uk/id/eprint/146179/>

This is the author's version of a work that was submitted to / accepted for publication.

Citation for final published version:

Omira, R., Baptista, M. A., Quartau, R., Ramalho, R. S., Kim, J., Ramalho, I. and Rodrigues, A. 2022. How hazardous are tsunamis triggered by small-scale mass-wasting events on volcanic islands? New insights from Madeira – NE Atlantic. *Earth and Planetary Science Letters* 578 , 117333. [10.1016/j.epsl.2021.117333](https://doi.org/10.1016/j.epsl.2021.117333)

Publishers page: <https://doi.org/10.1016/j.epsl.2021.117333>

Please note:

Changes made as a result of publishing processes such as copy-editing, formatting and page numbers may not be reflected in this version. For the definitive version of this publication, please refer to the published source. You are advised to consult the publisher's version if you wish to cite this paper.

This version is being made available in accordance with publisher policies. See <http://orca.cf.ac.uk/policies.html> for usage policies. Copyright and moral rights for publications made available in ORCA are retained by the copyright holders.



1 **How hazardous are tsunamis triggered by small-scale mass-wasting**  
2 **events on volcanic islands? New insights from Madeira – NE Atlantic**

3 R. Omira<sup>1,2,\*</sup>, M. A. Baptista<sup>2,3</sup>, R. Quartau<sup>4, 1</sup>, R. S. Ramalho<sup>5,1,6,7</sup>, J. Kim<sup>2</sup>, I. Ramalho<sup>1,2</sup>,  
4 A. Rodrigues<sup>4</sup>

5 <sup>(1)</sup> Instituto Dom Luiz (IDL), Faculdade de Ciências, Universidade de Lisboa, Lisbon, Portugal

6 <sup>(2)</sup> Instituto Português do Mar e da Atmosfera (IPMA), Lisbon, Portugal

7 <sup>(3)</sup> Instituto Superior de Engenharia de Lisboa, ISEL, Instituto Politécnico, Lisbon, Portugal

8 <sup>(4)</sup> Instituto Hidrográfico, Lisbon, Portugal

9 <sup>(5)</sup> School of Earth and Environmental Sciences, Cardiff University, Park Place, Cardiff, CF10 3AT,  
10 UK

11 <sup>(6)</sup> School of Earth Sciences, University of Bristol, Wills Memorial Building, Queen’s Road, Bristol  
12 BS8 1RJ, UK

13 <sup>(7)</sup> Lamont-Doherty Earth Observatory, Columbia University, Comer Geochemistry Building, PO  
14 Box 1000, Palisades, NY10964-8000, USA

15 \*Corresponding author: Rachid Omira (raomira@fc.ul.pt)

16 **Abstract**

17 Mass-wasting events are a key process in the evolution of volcanic ocean islands. They  
18 occur at various dimensional scales and present a major source of hazard. When the  
19 collapsed material plunges into the sea, destructive tsunamis can be generated. Yet, the  
20 hazard potential of collapse-induced tsunamis is still poorly understood with different  
21 opinions on what consequences to expect from this type of events, particularly those  
22 related to massive volcanic island flank collapses. In this paper, however, we explore the  
23 hazard extent of tsunamis triggered by the smaller – but more frequent – coastal cliff-  
24 failures, in order to isolate critical factors in the generation, propagation and impact of  
25 these tsunamis. To achieve this, we use the prime example of Madeira, a volcanic island  
26 in the Atlantic Ocean highly vulnerable to cliff-failure. Particularly, we explore the March  
27 4th, 1930 Cabo Girão event that triggered a deadly tsunami. The coastal impact of the  
28 1930 “Deadly Wave”, as the island’s inhabitants referred to the generated tsunami,  
29 resulted in 19 fatalities. We use historical description, morphological analysis, and  
30 numerical modelling to better understand the tsunamigenesis of tall island cliffs failing  
31 into the sea. Interestingly, we find that a relatively small-scale mass-wasting event

32 (~0.003 km<sup>3</sup> volume) was the cause of the reported tsunami that inundated the nearest  
33 coasts. Our numerical results, fairly agreeing with the available collapse and subsequent  
34 tsunami descriptions, suggest that the tsunami impact was mainly localized on the  
35 southern coast of Madeira Island. Furthermore, our study allows proposing a novel  
36 morphology-based conceptual model for the tsunamigenesis and hazard extent  
37 induced by mass-wasting events on oceanic volcanic islands.

38 **Keywords** – Mass-wasting, Volcanic islands, Tsunamigenesis, Hazard extent, Madeira  
39 Island, 1930 Cabo Girão tsunami, Atlantic.

## 40 **1. Introduction**

41 Volcanic ocean islands are very prominent and dynamic structures involving continuous  
42 stages of construction and destruction (e.g., McGuire, 1996; Ramalho et al., 2013).  
43 Throughout their lifecycles, mass-wasting events often interrupt the growth of the  
44 islands by removing significant parts of their edifices (e.g., Carracedo, 1996; Moore et  
45 al., 1994). These episodes present a major source of hazard in volcanic islands as they  
46 can involve large volumes of material and generate fast running debris avalanches  
47 (Siebert, 1992). If the failure material plunges into the sea, it can generate destructive  
48 tsunami that can potentially affect communities and infrastructure along low-lying  
49 coasts (e.g, McGuire, 2006).

50 Evidence of possibly catastrophic mass-wasting events in volcanic islands has been  
51 revealed in numerous studies (Moore et al., 1994; Carracedo 1999; Day et al., 1999;  
52 Quartau et al., 2018a). Some research works linked the collapses to the generation of  
53 tsunamis (McGuire, 2006; Paris et al., 2011; Watt et al., 2012; Omira et al., 2016a).  
54 Exceptionally, McMurtry et al. (2004), Pérez-Torrado et al. (2006), Paris et al. (2017), and  
55 Ramalho et al. (2015a) described deposits that attest to the impact of megatsunamis  
56 following catastrophic collapses of Mauna Loa (Hawaii), Tenerife (Canary Islands) and  
57 Fogo (Cape Verdes), respectively. Whilst their findings help unlock the debate on the  
58 potential of giant collapses to generate extreme tsunamis, it is still hard to draw a  
59 general conclusion on the tsunamigenesis of all collapses in oceanic islands. This is so  
60 because the volume of the material involved during the failure is not the only parameter

61 controlling the tsunamigenesis of flank collapses, but other factors (i.e., collapse process  
62 and dynamics) are highly influential.

63 A recent tsunami event involving a flank-collapse took place on December 22<sup>nd</sup>, 2018,  
64 following the eruption of the Anak Krakatau volcano in Indonesia (Paris et al., 2020; Grilli  
65 et al., 2021). The tsunami was generated when a sector of the island collapsed into the  
66 sea causing waves that struck along the rim of the Sunda Strait and resulted in 437  
67 fatalities and many coastal houses heavily damaged (Putra et al., 2020). This event  
68 demonstrated the capability of point-sourced tsunamis to impact coastal zones located  
69 tens of kilometres from the source area and raised the limitation of the warning systems  
70 in forecasting such “silent” tsunamis (Omira and Ramalho, 2020). Moreover, it showed  
71 how urgent it is to improve our scientific understanding of collapse-triggered tsunamis  
72 and their mechanisms, in order to better assess the hazard potential posed by these  
73 events, as well as their frequency and consequences. Crucially, the Anak Krakatau event  
74 also raised the conscience that the debate is often too centred on the very low  
75 probability, but very high impact events associated to giant island lateral collapses, and  
76 that the consequences of tsunami events triggered by smaller but much more frequent  
77 cliff-failures is not properly being considered.

78 Coastal cliff-failures are a ubiquitous process in the evolution of cliff-bounded coastlines  
79 and there are reasons to believe that – with rising sea levels and an increase in coastal  
80 erosion as result of global warming – they will become more frequent and consequently  
81 present a greater threat to coastal communities (Trenhaile, 2014). The issue of tsunamis  
82 triggered by coastal landslides is also especially relevant in the case of volcanic oceanic  
83 islands, as these are generally very prominent and unstable, and are particularly  
84 exposed to coastal erosion (Quartau et al., 2010; Ramalho et al., 2013; Melo et al., 2018;  
85 Huppert et al., 2020).

86 In few places of our planet the hazard posed by tsunamigenic cliff-failures is more acute  
87 than on the case of the Atlantic volcanic archipelagos, which are particularly prone to  
88 coastal mass-wasting (Quartau et al., 2010; Ramalho et al., 2013; Melo et al., 2018).  
89 Effectively, the Atlantic volcanic archipelagos of the Azores, Madeira, Canaries, Cape  
90 Verde and Tristan da Cunha feature some of the highest coastlines of any volcanic  
91 archipelagos in the world, with many of the islands being entirely cliff-bounded and

92 exhibiting near-vertical cliffs that frequently attain heights of 300–800 m. Why the  
93 Atlantic volcanic islands generally feature such high (and unstable) coastlines rest on a  
94 fortuitous combination of factors: these islands are, by nature, extremely prominent  
95 volcanoes (on account of being built of alkalic volcanic sequences); they are subjected  
96 to low rates of volcanic growth and often to low subsidence rates, which facilitates  
97 coastal erosion (Ramalho et al., 2013; Quartau et al., 2018b); and – crucially – they are  
98 unprotected by coral reefs and are exposed to the extremely energetic wave regime of  
99 the Atlantic Ocean (Rusu and Florin, 2016). It is this combination of factors that led to  
100 the formation of high cliffs such as the ones at the western coast of Corvo (up to 720 m),  
101 the northern shore of São Jorge (up to 945 m), the western shore of Flores (up to 580  
102 m), or the northern and western shores of Madeira (up to 500 m) (Fig. 1).

103 The instability of high coastal cliffs along the Atlantic islands is well attested by the  
104 presence of large coastal talus platforms – locally termed “fajãs” –, which result from  
105 the accumulation of landslide debris at the foot of the cliff and the adjacent island shelf  
106 – and also by the numerous and well documented historical cliff-failure events, many of  
107 which were tsunamigenic (Rodrigues, 2005; Andrade et al., 2006; Ramalho et al., 2013;  
108 Melo et al., 2018). Madeira Island is a particularly good case study, since its historical  
109 record is rich in eyewitness accounts of several mass-wasting events along its high  
110 coastal cliffs, namely in 1689, 1804, 1930, 1992, 1994 and 2008 CE (Rodrigues, 2005)  
111 (see Figs. 1c and 1d).

112 One of the better documented examples of a tsunamigenic cliff-failure in Madeira is the  
113 March 4<sup>th</sup>, 1930 event, which resulted from the failure of a sector of the Cabo Girão cliff,  
114 located in the southern shore (Fig. 1c). The collapsed material plunged into the sea and  
115 generated a local tsunami that propagated along Madeira’s southern coast and flooded  
116 the Vigário beach (Fig. 2 for location) at Câmara de Lobos, causing 19 casualties and 2  
117 missing people (Rodrigues, 2005). A more recent cliff-failure involving around  $1.8 \times 10^6$   
118 m<sup>3</sup> of material occurred in 1992 at Penha D’Água forming a small fajã with 300 m x 300  
119 m. It generated a small tsunami that had no consequences at the neighbouring  
120 coastlines (Fig. 1d).

121 The aims of this study are twofold: (1) to contribute to a better understanding of the  
122 tsunami hazard posed by small-scale cliff-failure events; (2) to test and refine the

123 application of state-of-the-art numerical modelling to generation, propagation and  
124 inundation of tsunamis triggered by small cliff-failures, here using the excellent case  
125 study provided by the 1930 cliff-failure tsunami. To achieve these aims, we use detailed  
126 historical description, morphological analysis, and evidence-calibrated numerical  
127 modelling of tsunami generation and propagation over a high-resolution digital  
128 bathymetric and topographic model. Our results are then explored to unlock, at least  
129 partially, the debate on the tsunamigenic potential and hazard extent of small-scale  
130 events frequently occurring on the flanks of ocean volcanic islands.

## 131 **2. Geological setting**

132 Madeira is the largest and youngest island of Madeira Archipelago (Fig. 1b), with a  
133 volcanic history extending from >7 Ma to the Holocene (Geldmacher et al., 2000;;  
134 Ramalho et al., 2015b). The island edifice is a prominent E-W elongated shield volcano  
135 that stands approximately 6 km above the surrounding seafloor, exhibiting an onshore  
136 area of 728 km<sup>2</sup> and presently attaining a maximum elevation of 1862 m above mean  
137 sea level, at Pico Ruivo. Despite its relatively young age, the island is deeply dissected by  
138 a dense river network, on account of torrential erosion driven by a high precipitation  
139 regime (Lira et al., 2013). The island was also the subject of large flank collapses – as  
140 demonstrated by a recent high-resolution multibeam bathymetric survey – which also  
141 contributed to increase the steepness of the volcanic edifice’s flanks (Quartau et al.,  
142 2018a). The island shelf is relatively wide, particularly on the northern (windward) and  
143 southwestern sectors where it extends, respectively, up to 6 and 9 km offshore (Quartau  
144 et al., 2018a).

145 The coastline of Madeira is generally cliff-bounded, featuring numerous nearly vertical  
146 cliffs that frequently reach in excess of 300 m and up to nearly 600 m in elevation. Such  
147 cliffs are usually cut in thick, largely effusive sequences, which – on account of intrinsic  
148 structural weakness derived by the prevalence of columnar jointing and alternation with  
149 more friable clinker and/or tephra layers – are prone to gravitational failure, triggering  
150 rockfalls, topples, debris avalanches and more rarely rotational landslides (Rodrigues  
151 2005; Ramalho et al., 2013). These landslides are responsible for the formation of  
152 coastal talus platforms, which – notwithstanding their vulnerability to wave erosion –

153 are a testimony to the relatively large volumes of collapsed material involved in these  
154 events.

155 Cabo Girão (32°39'23"N, 17°0'24"W) is a major landmark along the southern shore of  
156 the island, exhibiting a nearly vertical cliff of 589 m in elevation. The area has been the  
157 subject of numerous pre-historic and historic landslides, as it is discernible by the visible  
158 collapse scars on the cliff, and the talus accumulations of Fajã dos Padres (west of Cabo  
159 Girão proper) and Fajã dos Asnos (immediately below Cabo Girão), and Fajã das Bebras  
160 (east of Cabo Girão proper), which is the one that largely resulted from the March 4<sup>th</sup>,  
161 1930 event (see Fig. 2).

### 162 **3. Data and methods**

#### 163 **3.1. Retrieving the tsunami metrics from historical description**

164 For a better understanding of what happened on March 4<sup>th</sup>, 1930 along the coast of  
165 Madeira Island, we scrutinized the documents reporting the event and carefully  
166 analysed the available descriptions to retrieve quantitative characteristics of the  
167 generated tsunami and its impact. The newspapers "*Diário de Notícias*" n<sup>o</sup> 16678  
168 (*DN16678*) and "*Diário da Madeira*" n<sup>o</sup> 5569 (*DM5569*), both of March 6<sup>th</sup>, 1930, provide  
169 a compilation of the best available information on the Cabo Girão event. Additional  
170 descriptions of the cliff-failure and the resulting tsunami were also found in some  
171 recently published research works (Rodrigues, 2005; Baptista and Miranda, 2009). From  
172 these documents, we distinguished between information on the collapse mechanism,  
173 the tsunami generation, and the impact of the waves when reaching the coast.

##### 174 3.1.1. The Cabo Girão cliff-failure and tsunami generation

175 The landslide occurred on March 4<sup>th</sup>, 1930, at 9:20 am, local time. The mass split as a  
176 whole from the cliff face of Pico do Rancho, which is ~1.4 km to the ESE of Cabo Girão  
177 proper and is more than 350 m in height; it quickly disintegrated as it fell and the failure-  
178 involved material spread southwards. Simultaneously, a cloud made of dust was formed  
179 and then vanished westward, taken away by the strong breeze. The collapse led to the  
180 formation of a deposit (talus accumulation) that extended ~500 m towards the south  
181 (~200 m onshore and 300 m offshore) where it reached deep water and forming the

182 landform that became known as Fajã das Bebras (Fig. 2). The involved material consisted  
183 of a mixture of rocks (basaltic lava flow and tuff blocks) and some loose soil.

184 According to eyewitnesses, “following the collapse, an enormous wave of several  
185 meters, looking like a cloud, was formed and moved fast towards the village” of Câmara  
186 de Lobos (Vigário beach and village Bay). At the same time, a strong sea swirling was  
187 observed in an opposing direction of the wave propagation.

### 188 3.1.2. Tsunami impact on Madeira coast

189 The Vigário beach was the coastal zone dramatically struck by the tsunami waves. At the  
190 moment of the sector collapse, women were washing clothes in a small lagoon of the  
191 Vigário stream mouth approximately 50 m away from the shoreline, while their children  
192 were playing nearby. Just beyond the stream mouth, several men were working, and on  
193 the opposite side, some fishermen were preparing two boats before going fishing. The  
194 warning signal was given by the fishermen who first saw the incoming wave. The panic-  
195 stricken women ran to save their children, while others also tried to take the clothes  
196 they had spread on the pebbles. The river mouth in the Vigário beach was dramatically  
197 hit by the massive wave that dragged all who had no time to escape. When the wave  
198 receded, some women and children were seen among the foam and debris. From land,  
199 some men shouted for the women to grab the floating timber, but they couldn’t save  
200 themselves and their children due to the strong water current.

201 At the bay of Câmara de Lobos, a fisherman lost two fishing crafts. Despite having  
202 climbed a ramp of 15 m height, the fisherman and his co-workers were still caught by  
203 the wave. The fisherman’s house, where several families lived, was flooded through the  
204 window even though it is located at 15 m above sea level.

205 The Cabo Girão tsunami of 1930 resulted in 19 fatalities, 2 persons were reported  
206 missing and 6 were injured (Rodrigues, 2005). According to eyewitnesses, there was not  
207 a higher number of victims and loss of boats due to the ebbing tide and the rough sea  
208 that conditioned the regular fishermen activities the day of the event (DN16678).  
209 Reports indicated that approximately 50 persons were working in the beach at the  
210 time of the event (Rodrigues, 2005).



### 211 **3.2. Digital elevation model and landslide volume**

212 We gathered the best available topographic and bathymetric data to build an accurate  
213 high-resolution digital elevation model (DEM) for the area of interest. We obtained,  
214 from Direção Regional do Ordenamento do Território e Ambiente of the Regional  
215 Government of Madeira, the coastal topography and orthophotos with respectively 5 m  
216 and 0.4 m horizontal resolution (Figs. 2 d and 2e). Both data were based on vertical aerial  
217 photos acquired in 2007. The bathymetric data of nearshore water depths of 5- 10 m  
218 down to a depth of 100 m was provided by the Portuguese Hydrographic Office with a  
219 resolution of 10 m (Fig. 2e). This bathymetry was acquired in 2002 with a multibeam  
220 pole-mounted Simrad EM3000 system (Instituto Hidrográfico, 2003). To fill the gap  
221 between the coastline and the high-resolution bathymetry we used the lower resolution  
222 EMODNET bathymetry (<http://www.emodnet-bathymetry.eu>) based on single beam data.  
223 Bathymetric data deeper than 100 m was also based on the EMODNET bathymetry.  
224 Through the compilation of these datasets we obtained a 10 m resolution DEM that  
225 allowed a better representation of both bathymetric and topographic features of Cabo  
226 Girão and surrounding coastal areas, and consequently a detailed geomorphological  
227 analysis of this landslide.

228 For the sake of a higher consistency, we combined two methods to infer the volume of  
229 the studied landslide. The first one, relied on the reconstruction of the pre-failure  
230 topography by the simple interpolation of slopes that are immediately adjacent to the  
231 collapse scar (e.g., Völker, 2009); the landslide volume was then obtained by subtracting  
232 the present-day topography from this interpolated topographic surface (Fig. 3). The  
233 other way determined the volume of the landslide deposit by comparison with the  
234 surrounding bathymetry without cliff-failures deposits. We used the orthophotos and  
235 the bathymetry to map the extent of the failed deposit (including subaerial and  
236 submarine parts) (Fig. 2e). Landslide volumes obtained by these methods are depicted  
237 in Table 1. As both volume estimate methods present uncertainties mainly associated  
238 with the accuracy of the topographic and bathymetric available data, the precise  
239 identification of the landslide scar and deposit extent, and the morphic changes caused  
240 by erosion and deposition coastal processes, we averaged both volumes, obtaining  $2.87$   
241  $\times 10^6 \text{ m}^3$  (Table 1).

### 242 3.3. Tsunami numerical model

243 In this study we used a coupled depth-averaged two-layer model to simulate the mass-  
244 wasting movement and the tsunami it generates. The landslide is assumed as a  
245 viscoplastic deformable body and its downslope movement is simulated using the  
246 BingClaw model (Kim et al., 2019) that implements the Herschel-Bulkley rheology in a  
247 depth-integrated formulation. In the viscoplastic model, the landslide body is composed  
248 of two distinct zones: a shear deformable zone and a plug zone in which there is no  
249 deformation. BingClaw uses a finite volume numerical scheme to solve a system of a  
250 mass balance equation integrated over the entire flow depth and two separate  
251 momentum balance equations integrated over the depths of both the plug and shear  
252 zones.

253 For the numerical simulation of the Cabo Girão cliff-failure dynamics and the tsunami it  
254 generated, the densities of the landslide and water were set to  $1500 \text{ kg.m}^{-3}$  and  $1000$   
255  $\text{kg.m}^{-3}$ , respectively, and we tested various values of the yield stress ( $\tau_y$ ) to better mimic  
256 the deposited material. Parameterization of the landslide, scenarios tested and  
257 comparison of simulated deposits to observations are presented in Supplementary  
258 Material (S1). From these numerical tests, a yield stress of  $\tau_y = 10 \text{ kPa}$  was used in the  
259 simulation of the landslide downslope movement as it allows a better reproduction of  
260 the morphological features, mainly the landslide thickness and runout, of the identified  
261 deposit.

262 The tsunami generation, propagation and inundation are simulated using the GeoClaw  
263 model (Berger et al., 2011) that solves the nonlinear shallow water (NLSW) equations in  
264 a finite volume scheme. GeoClaw assumes a hydrostatic pressure and captures the  
265 propagation of breaking waves, bottom drag, and dry-wet inundation using a moving  
266 boundary (shoreline) algorithm. The validity of the NLSW model to properly simulate the  
267 Cabo Girão tsunami was investigated by comparing numerical results of both dispersive  
268 and non-dispersive models, as landslide-tsunami tends to develop dispersive behaviour  
269 while propagating from the source area towards the coast. Here, synthetic tsunami  
270 waveforms using both NLSW (e.g., Berger et al., 2011) and Boussinesq-type (e.g., Kim et  
271 al., 2017) models are compared at different water depth locations. Details of this  
272 comparative assessment are presented in Supplementary Material (S2). The models

273 show quite identical waveforms in the shallow water area (insular shelf) and very weak  
274 dispersive effects in the deep-water area (open ocean) and, therefore, non-dispersive  
275 tsunami model is considered applicable for our case study.

## 276 **4. Results and discussion**

### 277 **4.1. Structural and morphological conditions favouring cliff-failures at oceanic islands**

278 On volcanic islands, cliff instability and failure are particularly prevalent, as expected,  
279 along the windward or more exposed coasts of the volcanic edifices (if unprotected by  
280 coral reefs), where strong surf leads to faster wave erosion, cliff undercutting and a  
281 more effective erosion/transport of collapsed debris, leading to high and nearly vertical,  
282 often plunging seacliffs (Emery and Kuhn, 1982; Ramalho et al., 2013; Melo et al., 2018).  
283 The structure and composition of the cliffs – i.e., rock mass structure and strength – are  
284 also a critical factor in controlling cliff-failure and in determining the type (and volume)  
285 of landslides produced. For example, poorly unconsolidated pyroclastic sequences are  
286 friable and rapidly eroded but do not tend to generate tall cliffs and large landslides on  
287 account of their homogeneity and weakness. In contrast, the tallest cliffs and largest  
288 events of cliff-failure are generally associated with gently-dipping, largely effusive  
289 sequences, where simultaneously the hardness of materials leads to a higher resistance  
290 to erosion, but the heterogeneity of the materials and the pervasive columnar jointing  
291 of the lava flows promotes larger, vertically-propagating (from toe to crest) and less  
292 frequent failures, thus leading to a more episodic and threshold-driven failure behaviour  
293 (Ramalho et al., 2013; Melo et al., 2018). In these sequences, coastal retreat is chiefly  
294 the net result of a continuous horizontal erosive component provided by mechanical  
295 wave erosion and an episodic vertical erosive component provided by episodic mass  
296 wasting (Ramalho et al., 2013). In this respect, the cliffs of Cabo Girão are no exception  
297 and in fact constitute a good case study of how largely effusive (or mixed lava  
298 flow/pyroclastic) sequences are prone to develop tall nearly vertical cliffs and are  
299 subjected to episodic collapse.

300 In what concerns the triggering mechanisms for large cliff-failures, the situation is more  
301 complex. The stochastic behaviour of cliff-failures suggests that several mechanisms  
302 may contribute – and interact – to trigger failure events. There is no doubt that mechanic  
303 wave erosion and cliff undercutting/toe notching is a determining factor in creating the

304 conditions for failure, but what triggers the actual event is more enigmatic. Examples of  
305 large cliff-failures during or immediately after stormy conditions – when high rainfall and  
306 strong surf contribute to the rapid escalating of forces and the surpassing of threshold  
307 conditions – abound (e.g., Melo et al., 2018). It has been recognized that high rainfall  
308 followed by increased groundwater recharge may cause the gravitational loading and  
309 increased pore water pressure, resulting in reduced shear strengths that may result in  
310 failure (Stephensen, 2014; Dietze et al., 2020). The increase pounding of storm surf on  
311 plunging cliffs result in vibrations that may equally induce failure; in a similar fashion,  
312 earthquakes have been recognized as triggering significant coastal failures, as it happens  
313 in the tectonically active Azores Archipelago. Significant failures, however, were also  
314 registered during periods of fair weather or seismic quiescence, as it is the case of the  
315 1930 Cabo Girão and the 1992 Penha d'Águia landslides in Madeira. The triggering  
316 mechanism of large coastal cliff-failures is thus complex, non-linear and very difficult to  
317 predict, possibly resulting from a combination of factors which include toe notching,  
318 progressive fracture and facilitated connectivity from toe to crest, terrestrial controls on  
319 rock moisture, amongst other marine and subaerially controlled factors (Rosser et al.,  
320 2013). Given these considerations, the triggering mechanisms for the 1930 Cabo Girão  
321 landslide remain unknown, but a lesson to retain is that such events may happen  
322 without warning.

#### 323 **4.2. Pre-failure topography and tsunamigenesis of the Cabo Girão cliff**

324 Analysis of Figure 2 and 3 shows that the failure is initiated at an elevation of 350 m  
325 marking the top of the rim of the head-scar. The depositional area covers  $1.7 \times 10^5 \text{ m}^2$   
326 and is bounded at the top by the foot of the head-scar located at 50 m elevation and at  
327 the bottom by the foot of the landslide, located at 25 m of water depth (Fig. 3a). The  
328 landslide runout is up to 500 m with material deposited both on- and offshore (Figs. 2  
329 and 3).

330 In agreement with eyewitness observations of the 1930 event, our simulations show  
331 that the failure of Cabo Girão steep cliff into the sea, involving a volume of  $2.87 \times 10^6 \text{ m}^3$ ,  
332 leads to the generation of a tsunami. Figure 4 depicts the tsunami generation process,  
333 including the temporal evolution of the landslide mass movement (Figs. 4a to 4c) and

334 the ensuing wave formation (Figs. 4d to 4f). At  $t = 0$  sec the cliff-failure is initiated, and  
335 the evacuated material starts moving downslope (Figs. 4a and 4d). It immediately  
336 plunges into the sea (Fig. 4b) and perturbs the nearshore water column leading to the  
337 formation of a large wave of about 8 m in height (Figs. 4e). We find that the removed  
338 material moves fast down the steep cliff slope of  $\sim 78^\circ$ . It then encounters the shallow  
339 submarine platform with a gentle slope ( $\sim 2.5^\circ$ ) that slows down its movement. The  
340 landslide quickly reaches the steady state after 40 s of movement, exhibiting a runout  
341 distance up to 500 m (Fig. 4c), reproducing fairly the offshore deposit extension and  
342 geometry. At this stage, the resulting tsunami wave has a height of  $\sim 6$  m (Fig. 4f), in  
343 general agreement with eye-witness accounts. Our numerical results also show that a  
344 significant amount of the collapsed material is deposited on- and near-shore (Figs. 4c  
345 and 4f), in agreement with available eye-witness descriptions and morphological  
346 observations. This leads to a noticeable change in the shoreline configuration caused by  
347 the formation of a coastal talus-platform, which is also in agreement with the formation  
348 of what the locals named Fajã das Bebras, a landform that still exists albeit some marine  
349 erosion and coastal retreat since its formation (Figs. 2 and 3). Given these results, which  
350 match very well both the contemporaneous eyewitness accounts and the present-day  
351 morphological characteristics of the collapse scar and deposits, we are very confident  
352 that our numerical simulations reasonably reproduce the 1930 event and its effects,  
353 albeit some differences in the detail of matching the offshore deposit (see  
354 Supplementary Material S1) that we assume has no significant impact on the main  
355 results.

#### 356 **4.3. Tsunami propagation and hazard extent of the Cabo Girão event**

357 Unlike earthquake-triggered tsunamis that are generated by seafloor displacement  
358 typically in the open ocean (i.e., deep water) and then travel towards the coast, the Cabo  
359 Girão was a small- to moderate-sized point-sourced tsunami that was generated at the  
360 island coast and shelf, by a largely subaerial landslide falling in shallow water, which  
361 then propagated towards the open ocean and surrounding coastal areas. The tsunami  
362 energy pattern (in terms of max. wave heights) and inundation (in terms of max. flow  
363 depths) presented in Figure 5 provide useful insights into the hazard posed by the Cabo  
364 Girão cliff-failure tsunami. At the local scale, our simulations show that the tsunami

365 reached the nearest coastal areas immediately (few minutes) after the cliff-failure (Fig.  
366 5a). Here, at a first order, the simulated tsunami height is maximum (5-8 m, Fig. 5a) in  
367 the direction of the landslide movement. It then significantly decreases when  
368 propagating towards the deep water (1-2 m, Fig. 5a). Critically, our numerical  
369 simulations emphasize that the tsunami waves undergo a significant amplification over  
370 the inner part of the shelf, being maximum in both the western and eastern directions  
371 of the failure (arrows in Fig. 5a), rather than in the frontal area of the landslide, i.e., the  
372 shallow shelf guides the larger tsunami waves towards the nearest coasts. Among the  
373 affected coastal areas, the highest tsunami waves propagate towards the Vigário beach,  
374 where effectively most tsunami victims were reported. Here, the incident waves are as  
375 high as 4-5 m (Fig. 5b). Our simulations suggest that these waves caused the inundation  
376 of the entire Vigário beach with an estimated maximum flow depth of 4 m, an  
377 inundation distance up to 110 m, and a maximum runup height of 12 m (Fig. 5b). Whilst  
378 the simulated runup height at Vigário beach is comparable to that from the tsunami  
379 impact description (15 m, see Sect. 2.1), our numerical model slightly underestimates  
380 the maximum inundation distance. We believe that the use of the present-day coastal  
381 DEM for both the collapse area – which probably underestimates the landslide run in  
382 and volume – and the impacted coast (Vigário beach) influences the modelling results.  
383 The lack of detailed bathymetry on the shallowest areas of the shelf (technically very  
384 challenging to survey) may also have contributed to some inconsistency between the  
385 modelled and described hazard metrics.

386 At the regional scale, the tsunami energy seems to undergo a significant dissipation  
387 while the waves travel away from the source area and get around Madeira's coast (Fig.  
388 5c). According to our simulations, the tsunami arrived at the north-western coast of  
389 Madeira after 15 min of propagation with heights less than 0.2 m (Fig. 5c). Our results  
390 also show that the Desertas islands, located at ~ 18.5 km to the SE of Madeira, are only  
391 reached by a negligible tsunami wave (~ 5 cm) within 10 min, whilst no tsunami is  
392 observed at Porto Santo island, located at ~ 39.5 km to the NE of Madeira (Fig. 5c). These  
393 results confirm that the 1930 Cabo Girão tsunami was a point-source event of high local  
394 impact and very limited regional hazard extent, in agreement with eyewitness accounts.

395 Crucially, given that our numerical simulations were able to reproduce the historical  
396 event and its effects with a high degree of accuracy (notwithstanding some uncertainty  
397 in some parameters), this study demonstrates the utility of such approach to the  
398 investigation of the hazard posed by tsunamis triggered by the gravitational failure of  
399 tall plunging cliffs, thus opening an avenue for more detailed hazard studies. Moreover,  
400 this study emphasizes how state-of-the-art numerical modelling – made possible by  
401 high-resolution topographic/hydrographic datasets – may be used to better explore the  
402 relative vulnerability of coastlines to tsunamis triggered by near-field cliff-failures, with  
403 implications in terms of coastal engineering (e.g., in the design of tsunami-resilient  
404 coastal structures), territorial managements of coastal zones, civil protection, insurance  
405 policies, and disaster risk reduction.

#### 406 **4.4. Tsunamigenesis of small-scale mass-wasting events in volcanic islands**

407 The tsunamigenic potential of mass-wasting events has been recognized over the last 2-  
408 3 decades, but the failure mechanisms and dynamics leading to the formation of  
409 tsunamis, when the evacuated material plunges into the sea and moves downslope, are  
410 still poorly understood (Paris et al., 2018 and references therein). The lack of knowledge  
411 in this field primarily lies on the absence of direct and instrumental observations.  
412 Alternatively, the volume of the failure material, often inferred from mass transport  
413 deposits offshore and/or collapse scar onshore, is commonly considered as the main  
414 indicator of the tsunamigenesis of mass-wasting events. This applies to pre-historic  
415 catastrophic flank collapses involving tens to hundreds of cubic kilometres that were  
416 extensively studied in the Pacific Ocean (e.g., Hawaii, Moore et al., 1995; McMurty et  
417 al., 2014), Atlantic Ocean (e.g., Canary Islands and Cape Verde, Ward and Day, 2001;  
418 Paris et al., 2017; Barrett et al., 2020) and Indian Ocean (e.g., Krakatau, Maeno and  
419 Imamura, 2011) to establish link between their volume and the generation of  
420 “megatsunamis”. However, recent events such as Stromboli in December 2002 (Tinti et  
421 al., 2006) and Anak Krakatau in December 2018 (Paris et al., 2020; Grilli et al., 2021) have  
422 evidenced that small-scale collapses ( $< 0.5 \text{ km}^3$ ) are also capable of causing deadly  
423 tsunamis. Smaller scale events such as cliff-failures of the tall coastlines of volcanic  
424 islands in the NE Atlantic are relatively frequent (Cabral, 2009, Melo et al., 2018). These  
425 produce coastlines that are frequently bordered by these low-lying platforms where a

426 non-negligible part of the population of the islands live, have access to sea, or grow their  
427 crops. For instance, a similar event to the one studied here, occurred at Flores Island in  
428 the Azores; in 1857, a cliff-failure produced the fajã of Quebrada Nova with  $\sim 0.009 \text{ km}^3$ ,  
429 triggering a tsunami with a run-up of 5-7 m in Flores and the neighbouring Corvo Island,  
430 just  $\sim 22 \text{ km}$  apart. This tsunami injured  $\sim 100$  people, and caused 10 deaths in the two  
431 islands, all along the low-lying fajãs of these islands (Cabral, 2009). A more recent  
432 example is the November 14<sup>th</sup> 2020 cliff-failure at Gomera Island -Canary Islands- that  
433 caused a relatively small tsunami with wave heights in the range of 0.5 m reaching a  
434 village located 200 m away from the source (Galindo et al., 2021).

435 With these recent events in mind, there has been an increasing focus on the failure  
436 mechanism and dynamics of landslides as factors influencing the tsunami formation and  
437 hazard extent (Omira and Ramalho, 2020; Zengaffinen et al., 2020). A major source of  
438 uncertainty in the failure mechanism of flank sectors concerns their occurrence as a  
439 single or a sequence of multiple events, either in close succession or at a protracted  
440 timescale. Although insights into this feature can be inferred from detailed analyses of  
441 high-resolution post-event bathymetry, seismic reflection profiles and/or seismic  
442 stations records of mass movement, the availability of such data remains scarce.  
443 Understanding the dynamics of the collapse requires, on the other hand, real-time  
444 monitoring of the failure occurrence and its movement and/or accurate numerical  
445 modelling using in-situ determined physical and geotechnical properties of the material  
446 involved.

447 To our knowledge, less studied is the influence of the island coastal morphology in the  
448 tsunamigenic potential of sector collapses. In what concerns tsunamis triggered by  
449 smaller coastal cliff-failures, the island morphology – onshore and offshore – is a  
450 particularly determining factor in the dynamics of collapsed sectors and, therefore, on  
451 their tsunamigenesis and hazard extent. Such an effect is explored here through  
452 developing a conceptual tsunami formation model for two common coastal  
453 morphologies of ocean volcanic islands (Fig. 6).

454 Most oceanic volcanic islands exhibit insular shelves (i.e., shallow submarine platforms  
455 surrounding the islands), formed mostly by the combined effects of wave erosion of  
456 volcanic inactive coastlines, glacio-eustatic oscillations, and subsidence/uplift (Quartau



457 et al., 2010, 2018b; Ramalho et al., 2013). The presence of insular shelves conditions the  
458 dynamics of collapse emplacement and consequently of tsunami generation (Fig. 6, right  
459 panel). When cliffs fail into the sea the collapsed material encounters a shallow  
460 submarine platform with a gentle slope that decelerates its flow (Fig. 6b-c, right panel).  
461 This often leads to the deposition of an amount of the evacuated material within the  
462 shoreline resulting in an alteration of the coastal morphology and creation of a Fajã (Fig.  
463 6d, right panel). This particular process influences the tsunami generation as only a part  
464 of the collapsed material, i.e., effective landslide volume, continues moving over the  
465 shelf gentle slope displacing the water body and generating a solitary-like initial wave  
466 (Fig. 6b-c, right panel). Moreover, the generated wave will then propagate in the  
467 relatively shallow waters of the shelf – particularly on the wider shelves of older islands  
468 – experiencing dissipation towards the offshore but – critically – amplification along the  
469 shallower near-shore areas, causing significant damage to near-field shorelines.

470 In contrast, on islands subjected to: (a) vigorous active volcanism, where magma-supply  
471 rates result in accumulation rates at coastlines that exceed erosion rates, the  
472 progradation of coastal lava deltas is dominant (Mitchell et al., 2008; Quartau et al.,  
473 2015); (b) recent flank collapses and/or lava delta gravitational slumps (on coasts  
474 subjected to rapid volcanic progradation, Sansone and Smith, 2006; Bosman et al.,  
475 2014); and (c) calm waters and very low erosion rates, island shelves are not able to  
476 develop, resulting in steep submarine slopes down to the abyssal plains (Ramalho et al.,  
477 2013). On such coastlines (Fig. 6), the dynamics of the collapse is marked by large runout  
478 distances, resulting from a fast movement over a steep slope (Fig. 6, left panel). As the  
479 collapse material moves downslope, it continuously pumps energy into the water  
480 column leading to the formation of an initial N-wave with a large depression (Figs. 6b-c,  
481 left panel). This is also the case when large-scale island lateral collapses occur, which  
482 generally involve both the subaerial and the submarine parts of whole island flanks; in  
483 this case the existence or inexistence of the island shelf will not affect tsunamigenesis  
484 in any significant way as the collapse also includes the shelf.

485 In general, the ability of a tsunami to travel away from its source region relies on  
486 whether the generated wave contains enough energy to allow such an extent. For flank  
487 collapse-induced tsunamis the generation phase is completed when the sliding material

488 reaches the steady state. At this stage, the energy of the formed wave is composed of a  
489 potential energy  $E_p$  derived from the elevation of the free sea surface ( $\eta$ ) ( $E_p =$   
490  $\frac{1}{2} \int \rho g \eta^2 ds$ , where  $\rho$  is the density of water,  $g$  is the acceleration due to gravity, and  $ds$   
491 is the infinitesimal area element (Dutykh and Dias, 2009)) and a kinetic energy  $E_k$   
492 estimated from the wave speed ( $u$ ) ( $E_k = \frac{1}{2} \int \rho H u^2 ds$ , where  $\rho$  is the density of water,  $H$   
493 the total water depth, and  $ds$  is the infinitesimal area element (Dutykh and Dias, 2009)).  
494 In volcanic islands exhibiting insular shelves, the formed tsunami wave often loses a part  
495 of its  $E_p$  as the amount of the evacuated material involved in the formation of the fajã  
496 does not contribute to the disturbance of the nearshore water body. This process results  
497 in forming an initial wave (solitary-like) of relatively short wavelength and, therefore, of  
498 reduced  $E_p$ . A similar effect was revealed for tsunamis generated by large earthquakes  
499 on nearshore subduction zones, where a part of the co-seismic deformation occurs  
500 onshore and does not contribute to the wave generation (Omira et al., 2016b).  
501 Moreover, the presence of the insular shelf affects the  $E_k$  of the tsunami at both stages  
502 of generation and propagation. It decelerates the movement of both landslide and  
503 formed wave and channels the tsunami energy. The latter occurs due to the important  
504 exchange of  $E_k$  and  $E_p$  of waves trapped in the shelf, resulting in a locally focused tsunami  
505 impact while only waves with small heights escape the shallow area and propagate away  
506 from the source.

507 In clear contrast to events taking place on islands with surrounding shelves, both the  
508 loss of an amount of  $E_p$  of the triggered wave due to the formation of onshore morphic  
509 features and the shelf channelling of tsunami energy do not occur on oceanic islands  
510 without shelves (Figs. 6b-c, left panel). Here, the formed N-wave contains more energy  
511 pumped by the continuous and fast downslope movement of the evacuated material.  
512 Such generated tsunamis have more potential to travel away from the source area  
513 without remaining trapped in the shelf and dissipating energy in such a shallow morphic  
514 feature. The 1930 Madeira Island, studied here, and the 2018 Anak Krakatau tsunami  
515 events are prime examples supporting our conceptual model on the influence of the  
516 island submarine morphology on the tsunamigenesis and hazard extent of mass-  
517 wasting-triggered tsunamis. While the 1930 cliff-failure caused a solitary-type wave (see  
518 wave profiles in the Supplementary Material S3, Fig. S3.1) leading to a very limited

519 regional hazard extent (Fig. 5c), the 2018 Anak Krakatau collapse - regardless of its  
520 volume and failure mechanism that also involved a submarine part - occurred in a part  
521 of the island not surrounded by a shelf, triggering a relatively long N-wave tsunami (see  
522 wave profiles Supplementary Material S3, Fig. S3.2) that caused a regional impact on the  
523 Sunda Strait coasts (Putra et al., 2020).

524 Consequently, for the same volume involved in a costal cliff-failure event, the resulting  
525 wave characteristics will differ between the distinct islands' morphologies (Fig. 6), which  
526 could eventually lead to different tsunami hazard extents. This conceptual model should  
527 thus be considered when investigating the tsunamigenic hazard extent of small-scale  
528 coastal landslides.

## 529 **5. Conclusions**

530 This work contributes to unlock the debate on the tsunamigenic potential and hazard  
531 extent induced by small-scale mass-wasting events in oceanic volcanic islands. It  
532 benefits from the study of the prime example of Madeira -an island highly vulnerable to  
533 small mass-wasting and tsunami generation- and presents the first numerical  
534 investigation of the 1930 Cabo Girão cliff-failure and its ensuing tsunami. The numerical  
535 modelling results fairly reproduce the available description of the tsunami generation  
536 and coastal inundation, critically demonstrating the applicability of this approach to  
537 coastal vulnerability studies and for disaster risk reduction. They also demonstrate the  
538 high local and limited regional impact of such a point-source tsunami event. The detailed  
539 study of the 1930 event helps proposing a conceptional model that allows a better  
540 understanding of both the tsunamigenesis and tsunami hazard induced by small-scale  
541 mass-wating events occurring on distinct islands with distinct submarine morphological  
542 settings. The morphology-based model reveals a localized tsunami hazard for islands  
543 exhibiting insular shelves and greater potential of regional- to far-field tsunami impacts  
544 for islands without surrounding shelves. A proof of concept of the proposed model  
545 requires, however, extensive numerical testing of different coastal configurations and  
546 landslide volumes. Regardless of the island morphology, implementing forecast  
547 capabilities for such "silent" tsunami events remains an open challenge due to the  
548 absence of real-time monitoring and the short travel time of the waves to the  
549 threatened coasts.

550 **Acknowledgements**

551 This work is supported by projects MAGICLAND (PTDC/CTA-GEO/30381/2017),  
552 HAZARDOUS (PTDC/CTA-GEO/0798/2020) and UNTIeD (PTDC/CTA-GEO/28588/2017),  
553 funded by Fundação para a Ciência e a Tecnologia-FCT, I.P., the latter also being co-  
554 funded by the European Regional Development Fund, through POR Lisboa 2020. The  
555 authors acknowledge the financial support of FCT through project UIDB/50019/2020 –  
556 IDL. The authors wish to thank Victor Prior from IPMA for helping on the collection and  
557 interpretation of historical data and Duarte Costa at DSIGC-DROTA of the Regional  
558 Government of Madeira for providing the digital altimetry and ortophotos. R. Omira and  
559 R.S. Ramalho acknowledge their CEECIND/04876/2017 and IF/01641/2015 research  
560 contracts, respectively, funded by FCT. We finally thank the reviewer Raphaël Paris and  
561 the Editor Jean-Philippe Avouac for their encouraging comments that helped improving  
562 the paper.

563 **References**

- 564 Andrade, C., Borges, P., Freitas, M. C., 2006. Historical tsunami in the Azores archipelago  
565 (Portugal). *J. Volcanol. Geotherm. Res.* 156(1-2), 172-185.  
566 <https://doi.org/10.1016/j.jvolgeores.2006.03.014>.
- 567 Baptista, M. A., Miranda, J. M., 2009. Revision of the Portuguese catalog of tsunamis.  
568 *Nat. Hazards Earth Syst. Sci.* 9(1), 25-42. <https://doi.org/10.5194/nhess-9-25-2009>.
- 569 Barrett, R., Lebas, E., Ramalho, R., Klauke, I., Kutterolf, S., Klügel, A., Lindhorst, K., Gross,  
570 F. and Krastel, S., 2020. Revisiting the tsunamigenic volcanic flank collapse of Fogo Island  
571 in the Cape Verdes, offshore West Africa. *Geological Society, London, Special*  
572 *Publications* 500(1), 13-26. <https://doi.org/10.1144/SP500-2019-187>.
- 573 Berger, M. J., George, D. L., LeVeque, R. J., Mandli, K. T., 2011. The GeoClaw software  
574 for depth-averaged flows with adaptive refinement. *Adv. Water Resour.* 34(9), 1195–  
575 1206. <https://doi.org/10.1016/j.advwatres.2011.02.016>.
- 576 Bosman, A., Casalbore, D., Romagnoli, C., Chiocci, F., 2014. Formation of an ‘a’ā lava  
577 delta: insights from time-lapse multibeam bathymetry and direct observations during  
578 the Stromboli 2007 eruption. *Bull. Volcanol.* 76, 1-12. [https://doi.org/10.1007/s00445-](https://doi.org/10.1007/s00445-014-0838-2)  
579 [014-0838-2](https://doi.org/10.1007/s00445-014-0838-2).
- 580 Cabral, N., 2009. Análise do perigo de tsunamis nos Açores/Hazard assessment of  
581 tsunamis in the Azores. PhD thesis. Universidade dos Açores: Ponta Delgada. p. 170.
- 582 Carracedo, J. C., 1999. Growth, structure, instability and collapse of Canarian volcanoes  
583 and comparisons with Hawaiian volcanoes. *J. Volcanol. Geotherm. Res.* 94(1-4), 1-19.  
584 [https://doi.org/10.1016/S0377-0273\(99\)00095-5](https://doi.org/10.1016/S0377-0273(99)00095-5).
- 585 Carracedo, J. C., 1996. A simple model for the genesis of large gravitational landslide  
586 hazards in the Canary Islands. *Geological Society, London, Special Publications* 110(1),  
587 125-135. <https://doi.org/10.1144/GSL.SP.1996.110.01.10>.
- 588 Day, S. J., Da Silva, S. H., Fonseca, J. F. B. D., 1999. A past giant lateral collapse and  
589 present-day flank instability of Fogo, Cape Verde Islands. *J. Volcanol. Geotherm. Res.*  
590 94(1-4), 191-218. [https://doi.org/10.1016/S0377-0273\(99\)00103-1](https://doi.org/10.1016/S0377-0273(99)00103-1).
- 591 Dietze, M., Cook, K. L., Illien, L., Rach, O., Puffpaff, S., Stodian, I., & Hovius, N. (2020).  
592 Impact of nested moisture cycles on coastal chalk cliff failure revealed by multi seasonal  
593 seismic and topographic surveys. *Journal of Geophysical Research: Earth Surface*, 125,  
594 e2019JF005487. <https://doi.org/10.1029/2019JF005487>.
- 595 Dutykh, D., Dias, F., 2009. Energy of tsunami waves generated by bottom motion. *Proc.*  
596 *R. Soc. A* 465, 725–744. <https://doi.org/10.1098/rspa.2008.0332>.
- 597 Emery, K.O., Kuhn, G.G., 1982. Sea cliffs: their processes, profiles, and classification.  
598 *Geol. Soc. Am. Bull.* 93 (7), 644–654. [https://doi.org/10.1130/0016-](https://doi.org/10.1130/0016-7606(1982)93<644:SCTPPA>2.0.CO;2)  
599 [7606\(1982\)93<644:SCTPPA>2.0.CO;2](https://doi.org/10.1130/0016-7606(1982)93<644:SCTPPA>2.0.CO;2).
- 600 Geldmacher, J., van den Bogaard, P., Hoernle, K., Schmincke, H.-U., 2000. The <sup>40</sup>Ar/<sup>39</sup>Ar  
601 age dating of the Madeira Archipelago and hotspot track (eastern North Atlantic).  
602 *Geochem. Geophys. Geosyst.* 1, 1-26. <https://doi.org/10.1029/1999GC000018>.

603 Galindo, I., Romero, C., Martín-González, E., Vegas, J., Sánchez, N., 2021. A Review on  
604 Historical Tsunamis in the Canary Islands: Implications for Tsunami Risk Reduction.  
605 *Geosciences*, 11, 222. <https://doi.org/10.3390/geosciences11050222>.

606 Grilli, S.T., Zhang, C., Kirby, J.T., Grilli, A.R., Tappin, D.R., Watt, S.F.L., Hunt, J.E., Novellino,  
607 A., Engwell, S., Nurshal, M.E.M. and Abdurrachman, M., 2021. Modeling of the Dec. 22nd  
608 2018 Anak Krakatau volcano lateral collapse and tsunami based on recent field surveys:  
609 Comparison with observed tsunami impact. *Mar. Geol.* 440, 106566.  
610 <https://doi.org/10.1016/j.margeo.2021.106566>.

611 Huppert, K. L., Perron, J. T., Ashton, A. D., 2020. The influence of wave power on bedrock  
612 sea-cliff erosion in the Hawaiian Islands. *Geology* 48, 499-503.  
613 <https://doi.org/10.1130/G47113.1>.

614 Instituto Hidrográfico, 2003. Dinâmica Sedimentar da costa sul da ilha da Madeira.  
615 REL.TF.GM.02/03. Instituto Hidrográfico, Lisboa, Portugal., p. 161.

616 Kim, J., Løvholt, F., Issler, D., Forsberg, C. F., 2019. Landslide Material Control on Tsunami  
617 Genesis—The Storegga Slide and Tsunami (8,100 Years BP). *J. Geophys. Res., Oceans*  
618 124(6), 3607-3627. <https://doi.org/10.1029/2018JC014893>.

619 Kim, J., Pedersen, G.K., Løvholt, F., LeVeque, R.J., 2017. A Boussinesq type extension of  
620 the GeoClaw model—a study of wave breaking phenomena applying dispersive long wave  
621 models. *Coast. Eng.* 122, 75-86..<https://doi.org/10.1016/j.coastaleng.2017.01.005>.

622 Lira, C., Lousada, M., Falcão, A.P., Gonçalves, A. B., Heleno, S., Matias, M., Pereira, M. J.,  
623 Pina, P., Sousa, A. J., Oliveira, R., Almeida, A. B., 2013. The 20 February 2010 Madeira  
624 Island flash-floods: VHR satellite imagery processing in support of landslide inventory  
625 and sediment budget assessment. *Nat. Hazards Earth Syst. Sci.* 13, 709-719.  
626 <https://doi.org/10.5194/nhess-13-709-2013>.

627 Maeno, F., Imamura, F., 2011. Tsunami generation by a rapid entrance of pyroclastic  
628 flow into the sea during the 1883 Krakatau eruption, Indonesia. *J. Geophys. Res., Solid*  
629 *Earth* 116, B09205. <https://doi.org/10.1029/2011JB008253>.

630 McGuire, W. J., 2006. Lateral collapse and tsunamigenic potential of marine volcanoes.  
631 *Geological Society, London, Special Publications* 269(1), 121-140.  
632 <https://doi.org/10.1144/GSL.SP.2006.269.01.08>.

633 McGuire, W. J., 1996. Volcano instability: a review of contemporary themes. *Geological*  
634 *Society, London, Special Publications* 110(1), 1-23.  
635 <https://doi.org/10.1144/GSL.SP.1996.110.01.01>.

636 McMurtry, G. M., Fryer, G. J., Tappin, D. R., Wilkinson, I. P., Williams, M., Fietzke, J.,  
637 Garbe-Schoenberg, D., Watts, P., 2004. Megatsunami deposits on Kohala volcano,  
638 Hawaii, from flank collapse of Mauna Loa. *Geology* 32(9), 741-744.  
639 <https://doi.org/10.1130/G20642.1>.

640 Melo, C. S., Ramalho, R. S., Quartau, R., Hipólito, A. R., Gill, A., Borges, P. A., Cardigos, F.,  
641 Avila, S. P., Madeira, J., Gaspar, J. L., 2018. Genesis and morphological evolution of  
642 coastal talus-platforms (fajãs) with lagoon systems: the case study of the newly-formed

- 643 Fajã dos Milagres (Corvo Island, Azores). *Geomorphology* 310, 138-152.  
644 <https://doi.org/10.1016/j.geomorph.2018.03.006>.
- 645 Mitchell, N. C., Beier, C., Rosin, P. L., Quartau, R., Tempera, F., 2008. Lava penetrating  
646 water: Submarine lava flows around the coasts of Pico Island, Azores. *Geochem.*  
647 *Geophys. Geosyst.* 9(3), Q03024. <https://doi.org/10.1029/2007GC001725>.
- 648 Moore, J. G., Normark, W. R., Holcomb, R. T., 1994. Giant Hawaiian underwater  
649 landslides. *Science*, 264(5155), 46-48. <https://doi.org/10.1126/science.264.5155.46>.
- 650 Moore, J. G., Bryan, W. B., Beeson, M. H., Normark, W.R., 1995. Giant blocks in the South  
651 Kona landslide, Hawaii. *Geology* 23, 125-128. [https://doi.org/10.1130/0091-7613\(1995\)023<0125:GBITSK>2.3.CO;2](https://doi.org/10.1130/0091-7613(1995)023<0125:GBITSK>2.3.CO;2).
- 653 Omira, R., Quartau, R., Ramalho, I., Baptista, M. A., Neil, M., 2016a. The tsunami effects  
654 of a collapse of a volcanic island on a semi-enclosed basin: The Pico-São Jorge channel  
655 in the Azores archipelago. In *Plate Boundaries and Natural Hazards*, ISBN: 978-1-119-  
656 05397-2, (pp. 271-283). Eds: Duarte, J., and Schellart, W. American Geophysical Union  
657 (AGU), John Wiley & Sons. <https://doi.org/10.1002/9781119054146.ch13>.
- 658 Omira, R., Baptista, M. A., Lisboa, F., 2016b. Tsunami characteristics along the Peru–  
659 Chile trench: analysis of the 2015 Mw 8. 3 Illapel, the 2014 Mw 8. 2 Iquique and the 2010  
660 Mw 8. 8 Maule tsunamis in the near-field. *Pure Appl. Geophys.* 173(4):1063–1077.  
661 <https://doi.org/10.1007/s00024-016-1277-0>.
- 662 Omira, R., Ramalho, I., 2020. Evidence-calibrated numerical model of December 22,  
663 2018, Anak Krakatau flank collapse and tsunami. *Pure Appl. Geophys.* 177, 3059–3071.  
664 <https://doi.org/10.1007/s00024-020-02532-x>.
- 665 Paris, A., Heinrich, P., Paris, R., Abadie, S., 2020. The December 22, 2018 Anak Krakatau,  
666 Indonesia, landslide and tsunami: Preliminary modeling results. *Pure Appl. Geophys.*  
667 177, 571–590. <https://doi.org/10.1007/s00024-019-02394-y>.
- 668 Paris, R., Giachetti, T., Chevalier, J., Guillou, H., Frank, N., 2011. Tsunami deposits in  
669 Santiago Island (Cape Verde archipelago) as possible evidence of a massive flank failure  
670 of Fogos volcano. *Sediment. Geol.* 239(3-4), 129-145.  
671 <https://doi.org/10.1016/j.sedgeo.2011.06.006>.
- 672 Paris, R., Bravo, J. J. C., González, M. E. M., Kelfoun, K., Nauret, F., 2017. Explosive  
673 eruption, flank collapse and megatsunami at Tenerife ca. 170 ka. *Nat. Commun.* 8,  
674 15246. <https://doi.org/10.1038/ncomms15246>.
- 675 Paris, R., Ramalho, R. S., Madeira, J., Ávila, S., May, S. M., Rixhon, G., Engel, M., Brückner,  
676 H., Herzog, M., Schukraft, G. Perez-Torrado, F. J., 2018. Mega-tsunami conglomerates  
677 and flank collapses of ocean island volcanoes. *Mar. Geol.* 395, 168-187.  
678 <https://doi.org/10.1016/j.margeo.2017.10.004>.
- 679 Pérez-Torrado, F. J., Paris, R., Cabrera, M. C., Schneider, J.-L., Wassmer, P., Carracedo,  
680 J.-C., Rodríguez-Santana, Á., Santana, F., 2006. Tsunami deposits related to flank  
681 collapse in oceanic volcanoes: The Agaete Valley evidence, Gran Canaria, Canary Islands.  
682 *Mar. Geol.* 227, 135-149. <https://doi.org/10.1016/j.margeo.2005.11.008>.

683 Putra, P. S., Aswan, A., Maryunani, K. A., Yulianto, E., Nugroho, S. H., Setiawan, V., 2020.  
684 Post-Event Field Survey of the 22 December 2018 Anak Krakatau Tsunami. *Pure Appl.*  
685 *Geophys.* 177, 2477–2492. <https://doi.org/10.1007/s00024-020-02446-8>.

686 Quartau, R., Trenhaile, A.S., Mitchell, N.C., Tempera, F., 2010. Development of volcanic  
687 insular shelves: Insights from observations and modelling of Faial Island in the Azores  
688 Archipelago. *Mar. Geol.* 275, 66-83. <https://doi.org/10.1016/j.margeo.2010.04.008>.

689 Quartau, R., Madeira, J., Mitchell, N.C., Tempera, F., Silva, P.F., Brandão, F., 2015. The  
690 insular shelves of the Faial-Pico Ridge: a morphological record of its geologic evolution  
691 (Azores archipelago). *Geochem. Geophys. Geosyst.* 16, 1401–1420.  
692 <https://doi.org/10.1002/2015GC005733>.

693 Quartau, R., Ramalho, R. S., Madeira, J., Santos, R., Rodrigues, A., Roque, C., Carrara, G.,  
694 da Silveira, A. B., 2018a. Gravitational, erosional and depositional processes on volcanic  
695 ocean islands: Insights from the submarine morphology of Madeira Archipelago. *Earth*  
696 *Planet. Sci. Lett.* 482, 288-299. <https://doi.org/10.1016/j.epsl.2017.11.003>.

697 Quartau, R., Trenhaile, A.S., Ramalho, R.S., Mitchell, N.C., 2018b. The role of subsidence  
698 in shelf widening around ocean island volcanoes: Insights from observed morphology  
699 and modeling. *Earth Planet. Sci. Lett.* 498, 408-417.  
700 <https://doi.org/10.1016/j.epsl.2018.07.007>.

701 Ramalho, R. S., Winckler, G., Madeira, J., Helffrich, G. R., Hipólito, A., Quartau, Adena,  
702 K., Schaefer, J. M., 2015a. Hazard potential of volcanic flank collapses raised by new  
703 megatsunami evidence. *Sci. Adv.* 1(9), e1500456.  
704 <https://doi.org/10.1126/sciadv.1500456>.

705 Ramalho, R. S., Brum da Silveira, A., Fonseca, P., Madeira, J. Cosca, M., Cachão, M.,  
706 Fonseca, M., Prada, S., 2015b. The emergence of volcanic oceanic islands on a slow-  
707 moving plate: the example of Madeira Island, NE Atlantic. *Geochem. Geophys. Geosyst.*  
708 522–537. <https://doi.org/10.1002/2014GC005657>.

709 Ramalho, R. S., Quartau, R., Trenhaile, A. S., Mitchell, N. C., Woodroffe, C. D., Avila, S. P.,  
710 2013. Coastal evolution on volcanic oceanic islands: A complex interplay between  
711 volcanism, erosion, sedimentation, sea-level change and biogenic production. *Earth-Sci.*  
712 *Rev.* 127, 140-170. <https://doi.org/10.1016/j.earscirev.2013.10.007>.

713 Rodrigues, D. M. M., 2005. Análise de risco de movimentos de vertente e ordenamento  
714 do território na Madeira: aplicação ao caso de Machico. PhD thesis. Universidade da  
715 Madeira, Funchal, p. 382.

716 Rosser, N.J., Brain, M.J., Petley, D.N., Lim, M. and Norman, E.C., 2013. Coastline retreat  
717 via progressive failure of rocky coastal cliffs. *Geology*, 41(8), pp.939-942.

718 Rusu, E., Onea, F., 2016. Estimation of the wave energy conversion efficiency in the  
719 Atlantic Ocean close to the European islands. *Renewable Energy* 85, 687-703.

720 Sansone, F. J., Smith, J. R., 2006. Rapid mass wasting following nearshore submarine  
721 volcanism on Kilauea volcano, Hawaii. *J. Volcanol. Geotherm. Res.* 151(1-3): 133-139.  
722 <https://doi.org/10.1016/j.jvolgeores.2005.07.026>.



- 723 Siebert, L., 1992. Threats from debris avalanches. *Nature* 356(6371), 658-659.  
724 <https://doi.org/10.1038/356658a0>.
- 725 Stephenson, W. (2014). Rock coasts (first edition). In D. Masselink & R. Gehrels (Eds.),  
726 Coastal environments and global change (pp. 256–379). John Wiley & Sons.
- 727 Tinti, S., Pagnoni, G. and Zaniboni, F., 2006. The landslides and tsunamis of the 30th of  
728 December 2002 in Stromboli analysed through numerical simulations. *Bull.*  
729 *Volcanol.* 68(5), 462-479. <https://doi.org/10.1007/s00445-005-0022-9>.
- 730 Trenhaile, A. S., 2014. Climate change and its impact on rock coasts. Chapter 2 in *Rock*  
731 *Coast Geomorphology: A Global Synthesis*, Eds: D.M. Kennedy, W. J. Stephenson, and  
732 L. A. Naylor. Geological Society, London, *Memoirs* 40, 7-17.  
733 <https://doi.org/10.1144/M40.2>.
- 734 Völker, D. J., 2010. A simple and efficient GIS tool for volume calculations of submarine  
735 landslides. *Geo-Mar. Lett.* 30, 541-547. <https://doi.org/10.1007/s00367-009-0176-0>.
- 736 Ward, S. N., Day, S., 2001. Cumbre Vieja Volcano—potential collapse and tsunami at La  
737 Palma, Canary Islands. *Geophys. Res. Lett.* 28, 3397–3400.  
738 <https://doi.org/10.1029/2001GL013110>.
- 739 Watt, S. F. L., Talling, P. J., Vardy, M. E., Heller, V., Hühnerbach, V., Urlaub, M., Sarkar,  
740 S., Masson, D. G., Henstock, T. J., Minshull, T. A., Paulatto, M., 2012. Combinations of  
741 volcanic-flank and seafloor-sediment failure offshore Montserrat, and their implications  
742 for tsunami generation. *Earth Planet. Sci. Lett.* 319, 228-240.  
743 <https://doi.org/10.1016/j.epsl.2011.11.032>.
- 744 Zengaffinen, T., Løvholt, F., Pedersen, G.K. and Muhari, A., 2020. Modelling 2018 Anak  
745 Krakatoa flank collapse and tsunami: Effect of landslide failure mechanism and dynamics  
746 on tsunami generation. *Pure Appl. Geophys.* 177(6), 2493-2516.  
747 <https://doi.org/10.1007/s00024-020-02489-x>.

748 **Figure captions**

749 **Fig. 1.** (a) Overview of the NE Atlantic region where the main volcanic archipelagos stand;  
750 (b) Madeira Island within Madeira Archipelago, an island bound by high cliffs and prone  
751 to mass-wasting episodes; (c) Location of historical mass-wasting events occurred on the  
752 flanks of Madeira Island: Ponta do Sol (PS), Cabo Girão (CG), Penha D'Água (PA), Arco S.  
753 Jorge (AJ), and Seixal (Se); d) Photo of the 1992 Penha d'Água mass-wasting event and  
754 the tsunami it generated (Source: <http://aprenderamadeira.net/pedra-natural/>).  
755 Bathymetric and topographic data used to produce the maps are from EMODNET  
756 (Source: <https://www.emodnet-bathymetry.eu/>).

757 **Fig. 2.** Reconstruction of the cliff-failure of Cabo Girão in 1930 (a) Men extracting sand  
758 at the Vigário beach in the 30s of the 20<sup>th</sup> Century, about 100 m away from the failure  
759 site; (b) Women and children washing clothes at the Vigário beach (photos are available  
760 from: [http://www.concelhodecamaradelobos.com/dicionario/praias\\_vigario.html](http://www.concelhodecamaradelobos.com/dicionario/praias_vigario.html)); (c)  
761 Panoramic photo (dated of 8<sup>th</sup> December 2004) of the cliff at Cabo Girão, showing the  
762 landslide scar at the cliff face of Pico do Rancho and the resulting talus accumulation that  
763 became known as Fajã das Bebras; the highest point of the collapse scar is at ~350 m in  
764 elevation; (d) Orthophoto of the area, showing the offshore extent of the talus  
765 accumulation, which is approximately 500 m from the cliff base; (e) The same image of  
766 (d) but showing the DEM's used in the reconstruction (see section 3.2 for details).

767 **Fig. 3.** Elevation model of Cabo Girão: a) Post-event (present day) bathymetric and  
768 topographic model including the main morphologic features of the Cabo Girão cliff-  
769 failure; b) Pre-event elevation model showing the reconstruction of the Cabo Girão  
770 landslide; c) cross-section of both pre- and post-failure elevation models of Cabo Girão  
771 cliff.

772 **Fig. 4.** Simulations of Cabo Girão cliff-failure dynamics and tsunami generation: a) to c)  
773 Snapshots of the downslope mass failure movement; d) to f) Snapshots of tsunami  
774 generation, black dashed contours mark the landslide limits. CG, Cabo Girão; and VB,  
775 Vigário Beach.

776 **Fig. 5.** Cabo Girão point-sourced tsunami hazard extent: a) local-scale tsunami maximum  
777 wave height and travel time (contours each 20 sec); b) tsunami inundation at Vigário

778 beach; c) regional-scale tsunami maximum wave height and travel time (contours each  
779 1 min).

780 **Fig. 6.** Morphology-based conceptual model of tsunamigenic potential of small-scale  
781 mass-wasting events on volcanic islands flanks.

782

783 **Tables**

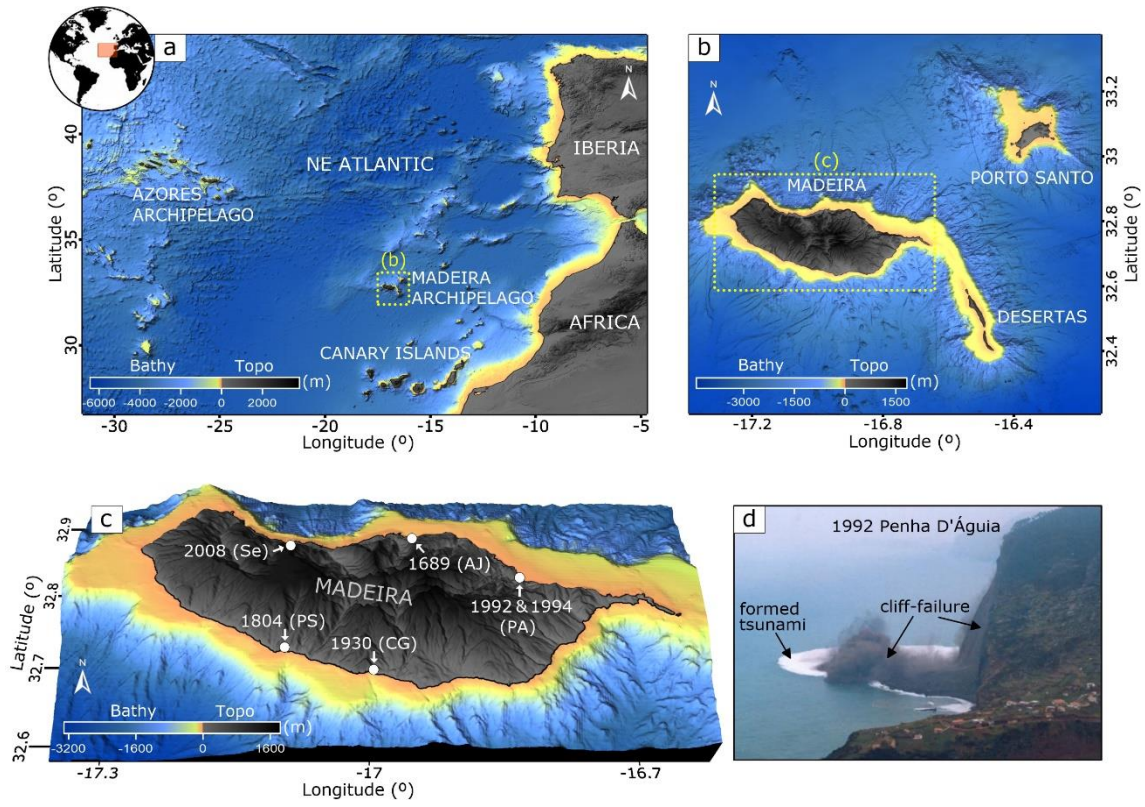
784 **Table 1.** Volume estimate of the 1930 Cabo Girão landslide in Madeira Island

Scar-derived volume (m <sup>3</sup> )	Deposit-derived volume (m <sup>3</sup> )	Averaged volume (m <sup>3</sup> )
2.895 x 10 <sup>6</sup>	2.845 x 10 <sup>6</sup>	2.87 x 10 <sup>6</sup>

785

786

787 **Figure 1**

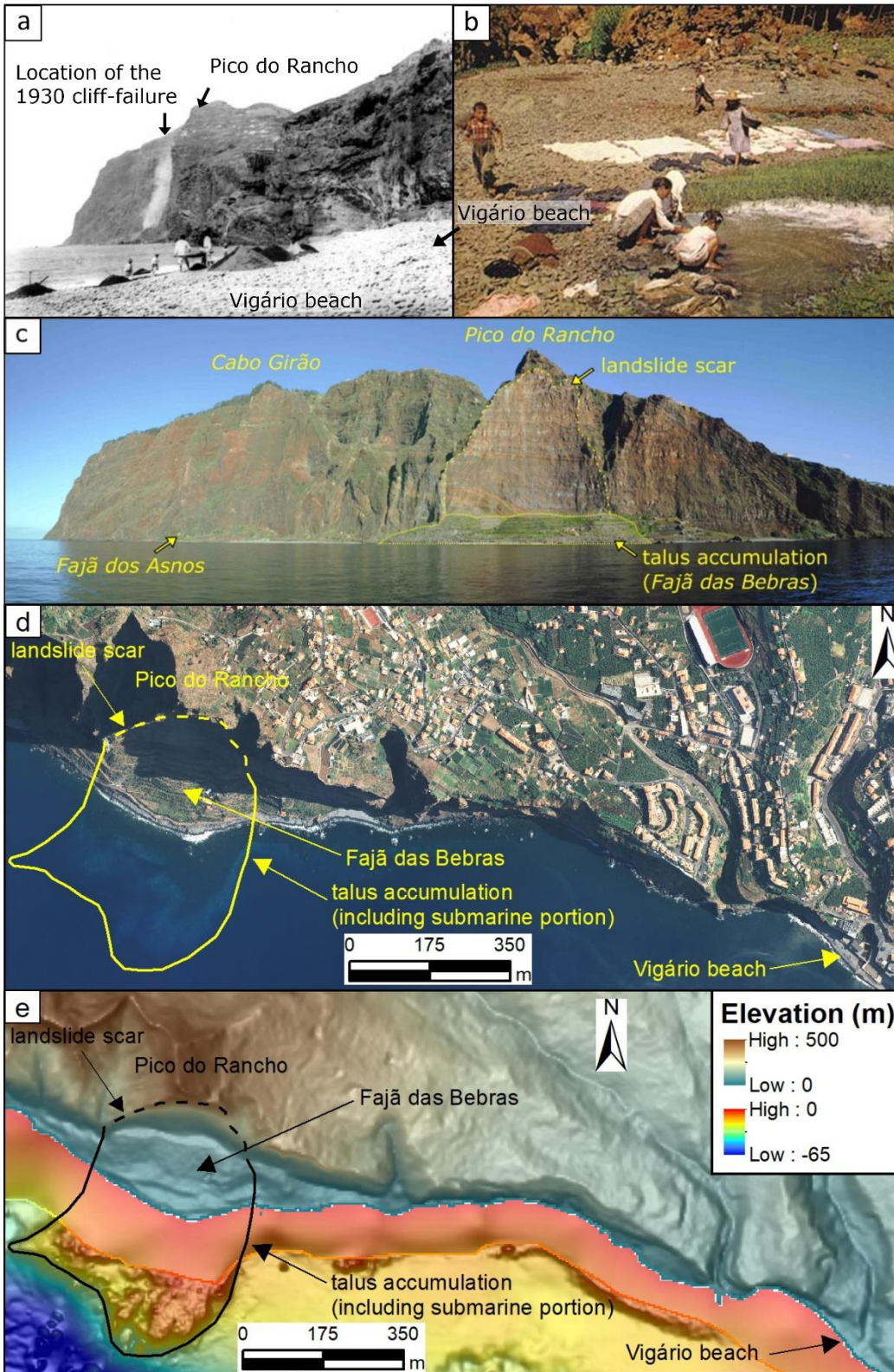


788

789

790

791 **Figure 2**



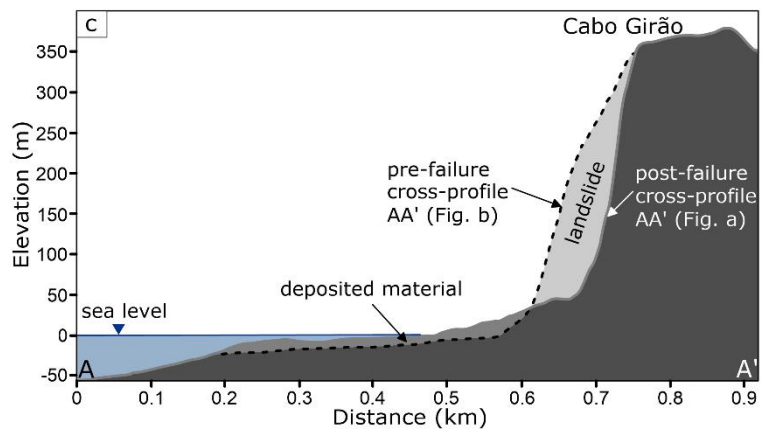
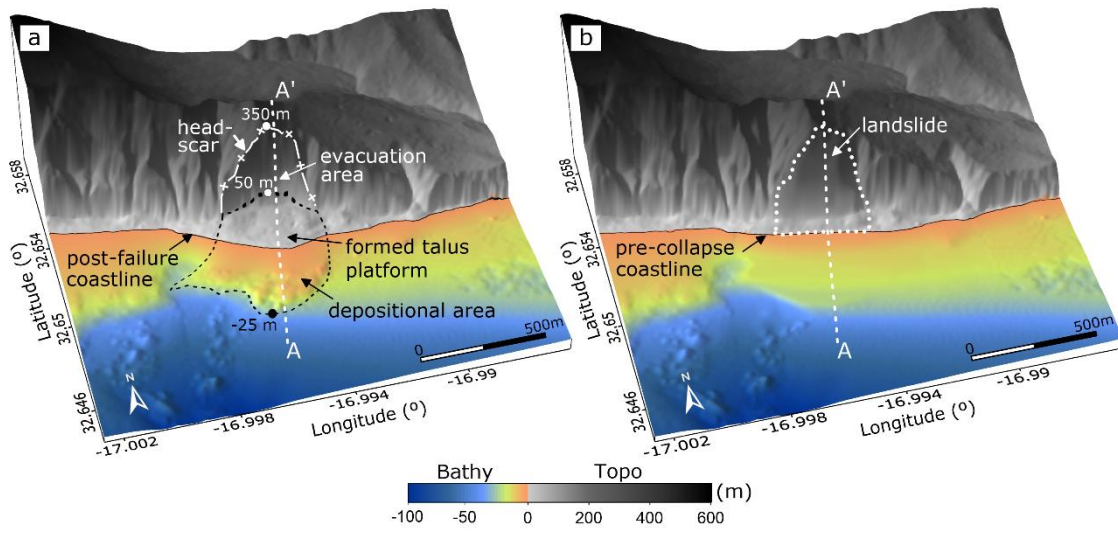
792

793

794

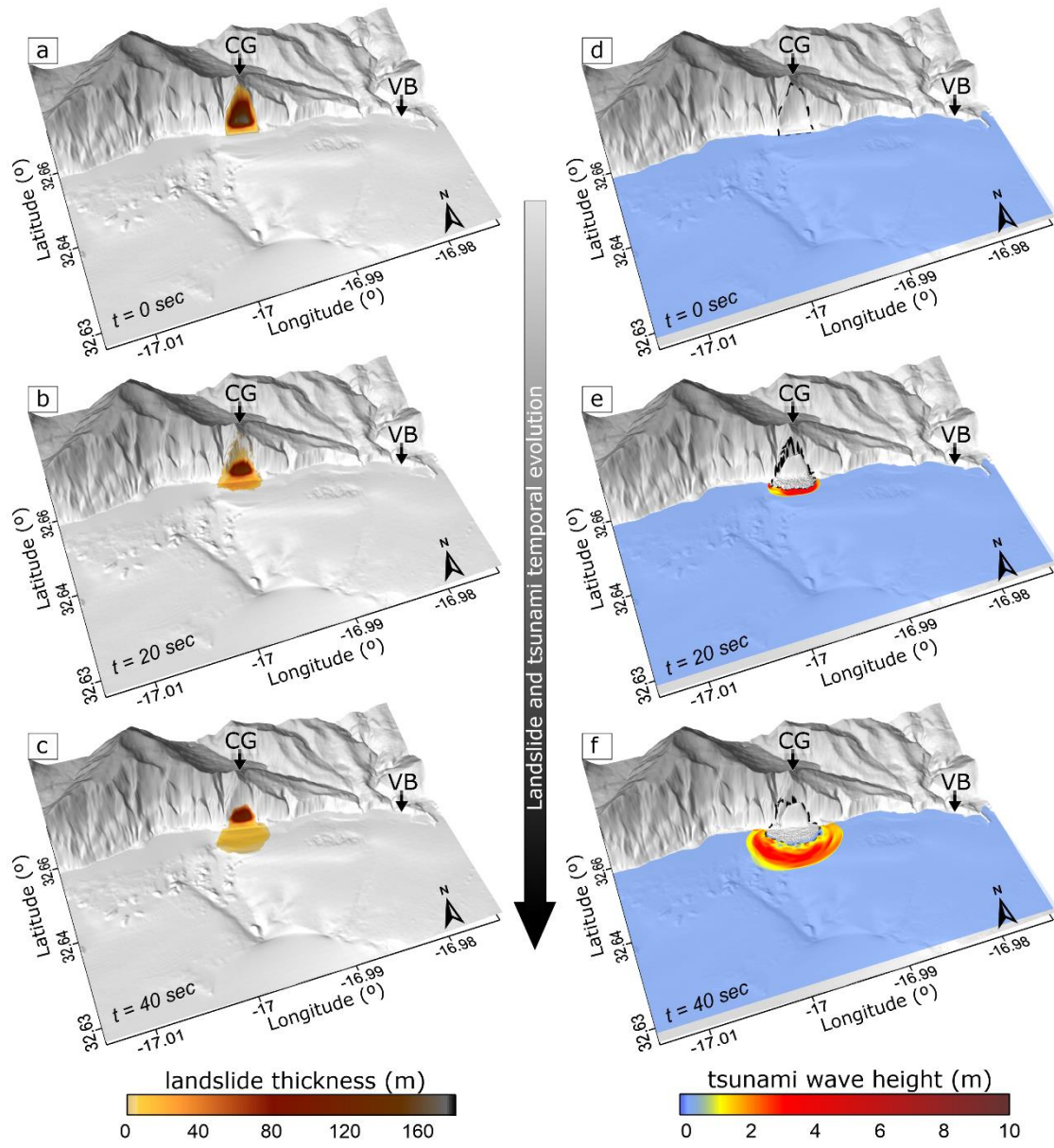
795

796 **Figure 3**



797

798



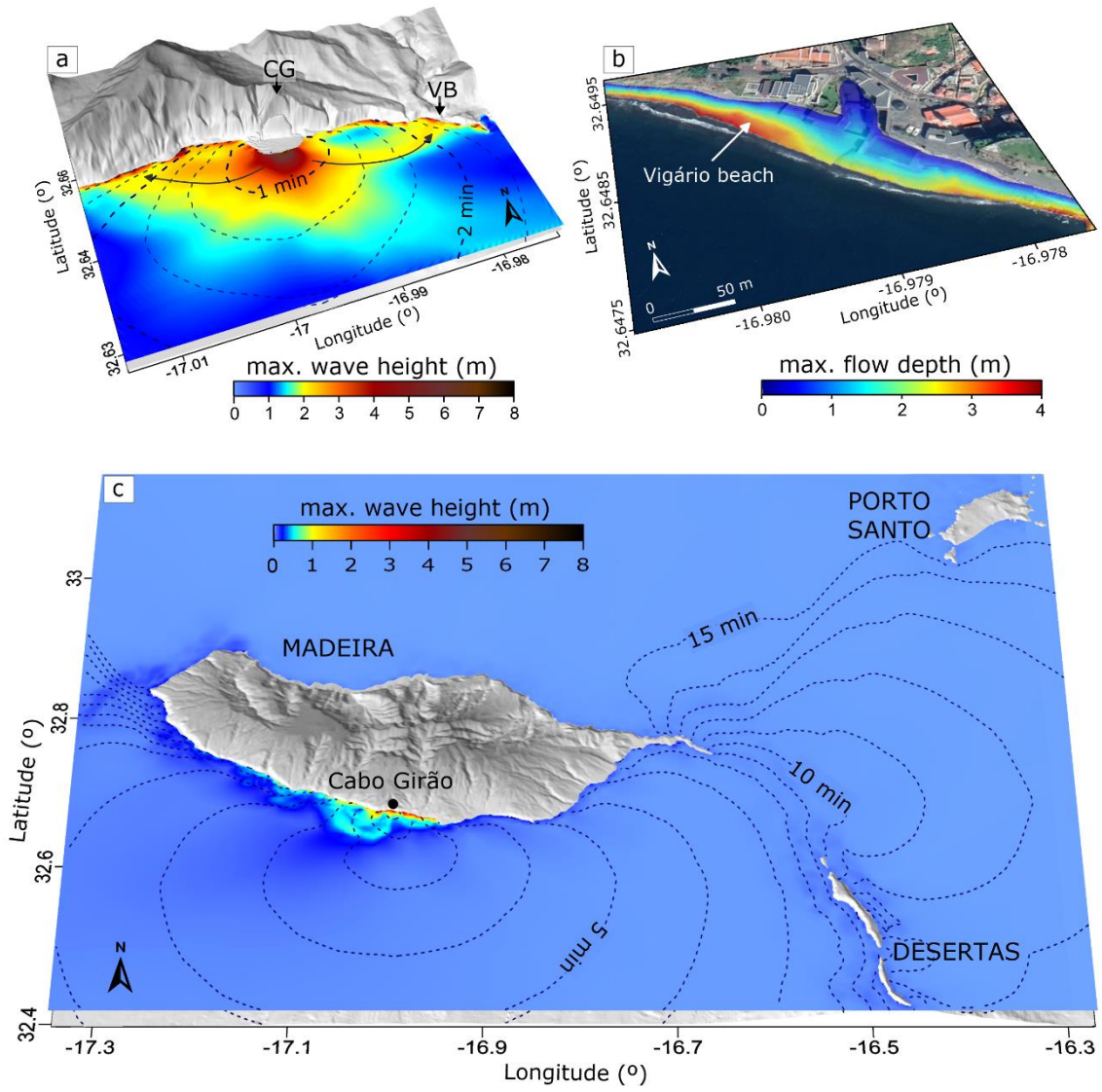
800

801

802



803 **Figure 5**

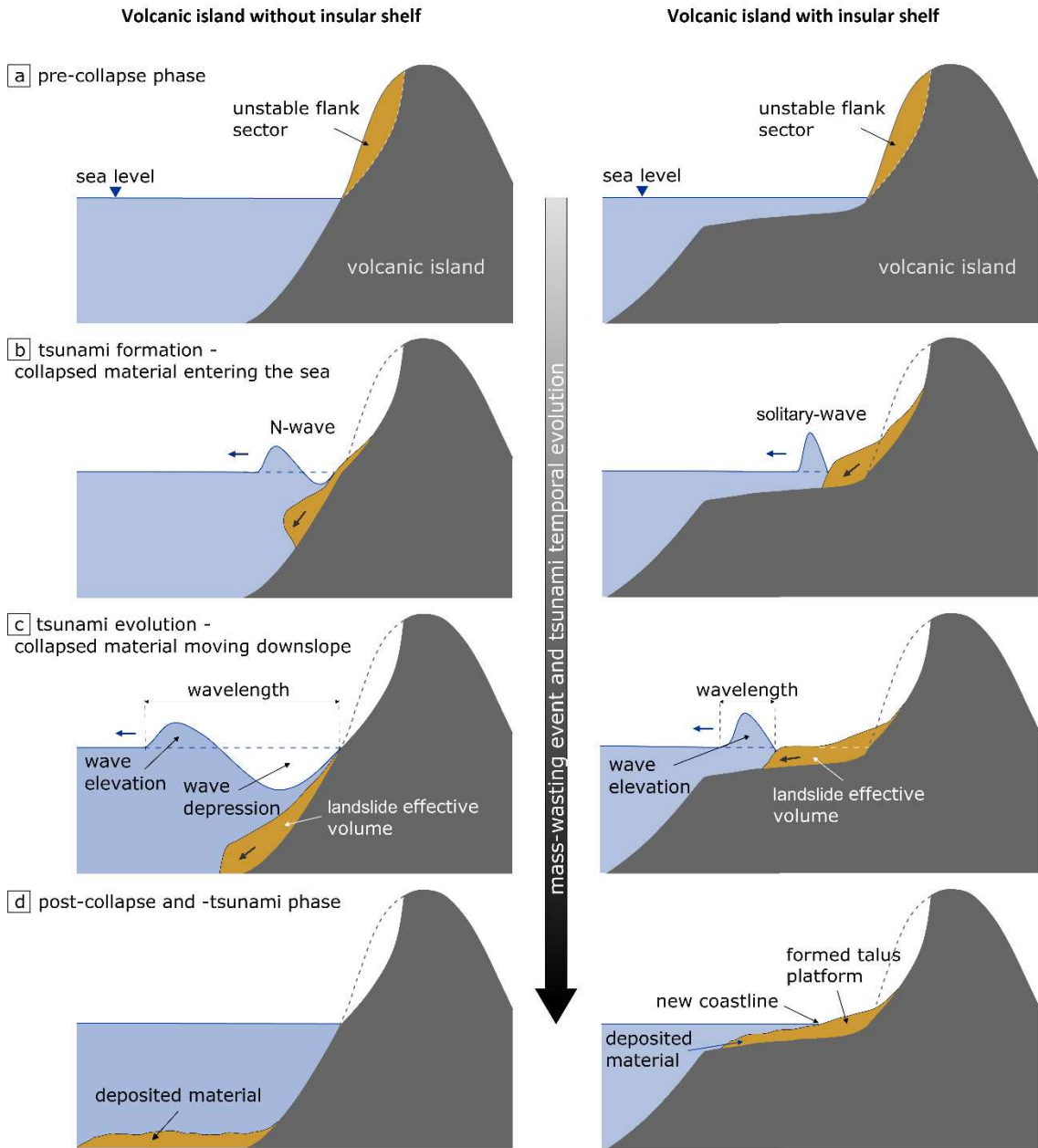


804

805

806

**Figure 5**





## **Supplementary Material**

### **How hazardous are tsunamis triggered by small-scale mass-wasting events on volcanic islands? New insights from Madeira – NE Atlantic**

R. Omira<sup>1,2,\*</sup>, M. A. Baptista<sup>2,3</sup>, R. Quartau<sup>4, 1</sup>, R. S. Ramalho<sup>5,1,6,7</sup>, J. Kim<sup>2</sup>, I. Ramalho<sup>1,2</sup>, A. Rodrigues<sup>4</sup>

(<sup>1</sup>) Instituto Dom Luiz (IDL), Faculdade de Ciências, Universidade de Lisboa, Lisbon, Portugal

(<sup>2</sup>) Instituto Português do Mar e da Atmosfera (IPMA), Lisbon, Portugal

(<sup>3</sup>) Instituto Superior de Engenharia de Lisboa, ISEL, Instituto Politécnico, Lisbon, Portugal

(<sup>4</sup>) Instituto Hidrográfico, Lisbon, Portugal

(<sup>5</sup>) School of Earth and Environmental Sciences, Cardiff University, Park Place, Cardiff, CF10 3AT, UK

(<sup>6</sup>) School of Earth Sciences, University of Bristol, Wills Memorial Building, Queen's Road, Bristol BS8 1RJ, UK

(<sup>7</sup>) Lamont-Doherty Earth Observatory, Columbia University, Comer Geochemistry Building, PO Box 1000, Palisades, NY10964-8000, USA

\*Corresponding author: Rachid Omira ([raomira@fc.ul.pt](mailto:raomira@fc.ul.pt))

## S1. Parameterization of the collapse and model comparison to observation

**Table S1.1:** Parameters of the landslide scenarios

Scenario	Volume (m <sup>3</sup> )	Density (kg.m <sup>-3</sup> )	Yield stress (kPa)	Time the landslide reaches the steady state (s) (from the model Fig S1.1)
Sce#1	2.87 x 10 <sup>6</sup>	1500	5.0	105.0
Sce#2	2.87 x 10 <sup>6</sup>	1500	10.0	40.0
Sce#3	2.87 x 10 <sup>6</sup>	1500	20.0	30.0
Sce#4	2.87 x 10 <sup>6</sup>	1500	30.0	10.0

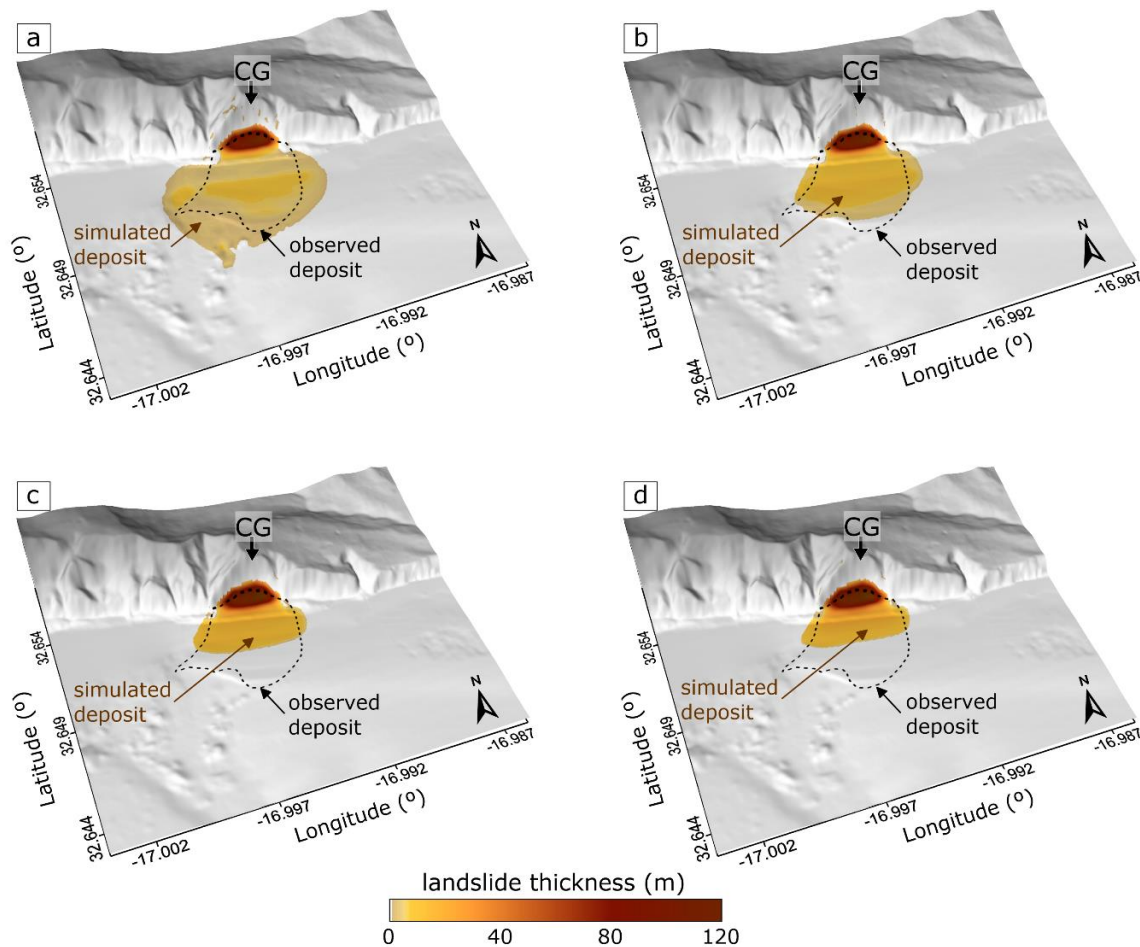


**Fig S1.1:** Comparison of modelled landslide deposit to the observed deposit for the different Cabo Girão (CG) cliff-failure scenarios listed in Table S1.1: **a)** Sce#1, **b)** Sce#2, **c)** Sce#3, and **d)** Sce#4.

## S2. Comparison of dispersive and non-dispersive models for the simulation of the 1930 Cabo Girão tsunami

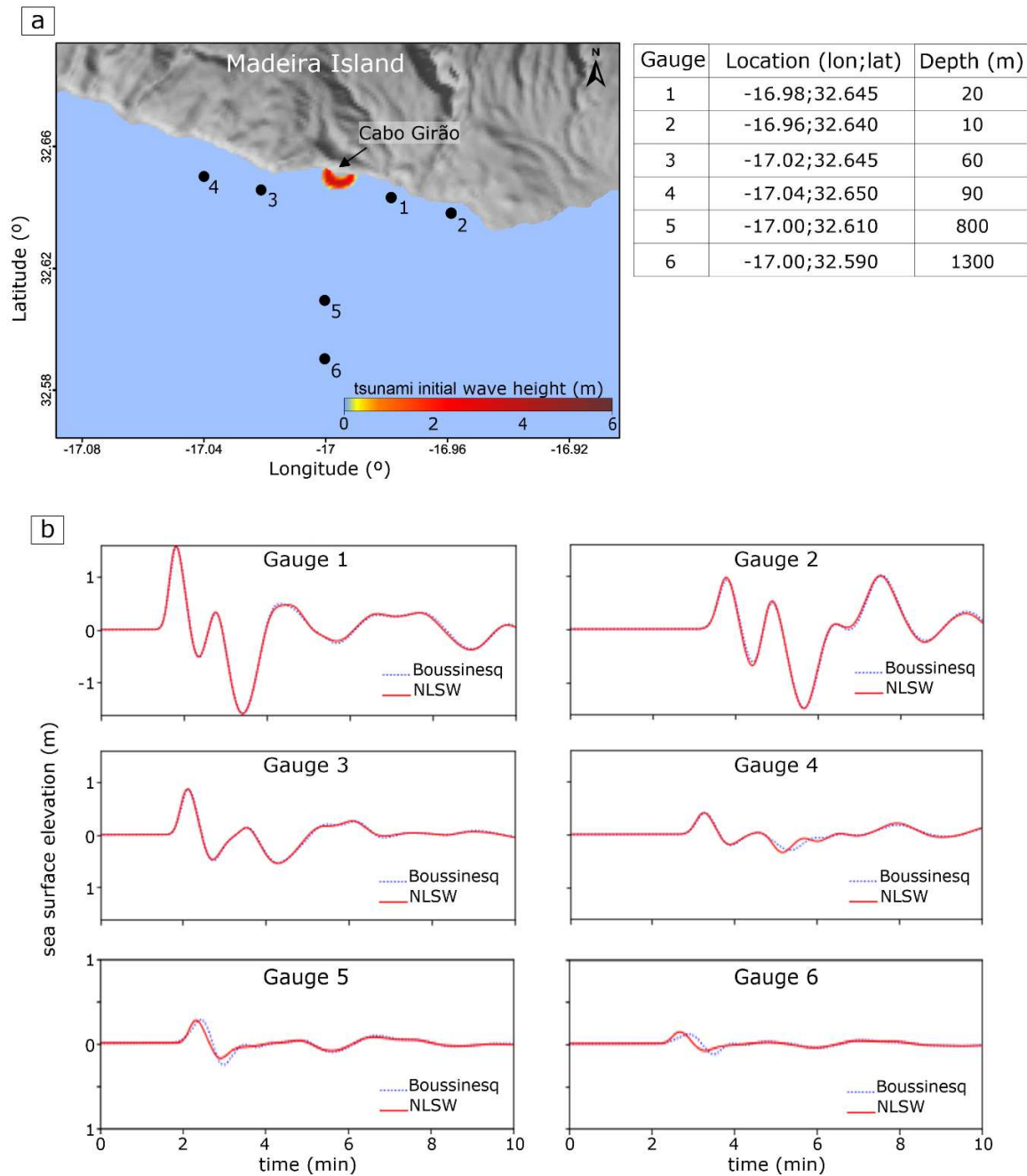


**Fig S2.1:** Comparison between non-dispersive (nonlinear shallow water-NLSW) and dispersive (Boussinesq) models in simulating the 1930 Cabo Girão, Madeira tsunami. **a)** plot of the localities (Gauges) where the simulated tsunami waveforms are compared (left panel) and their exact locations and depths (table, right panel); **b)** comparison, at each gauge, of the synthetic waveforms obtained from both NLSW and Boussinesq models simulations.

**S3. On the wave characteristics of the tsunamis generated by the 1930 Madeira cliff-failure and the 2018 Anak Krakatau flank-collapse**

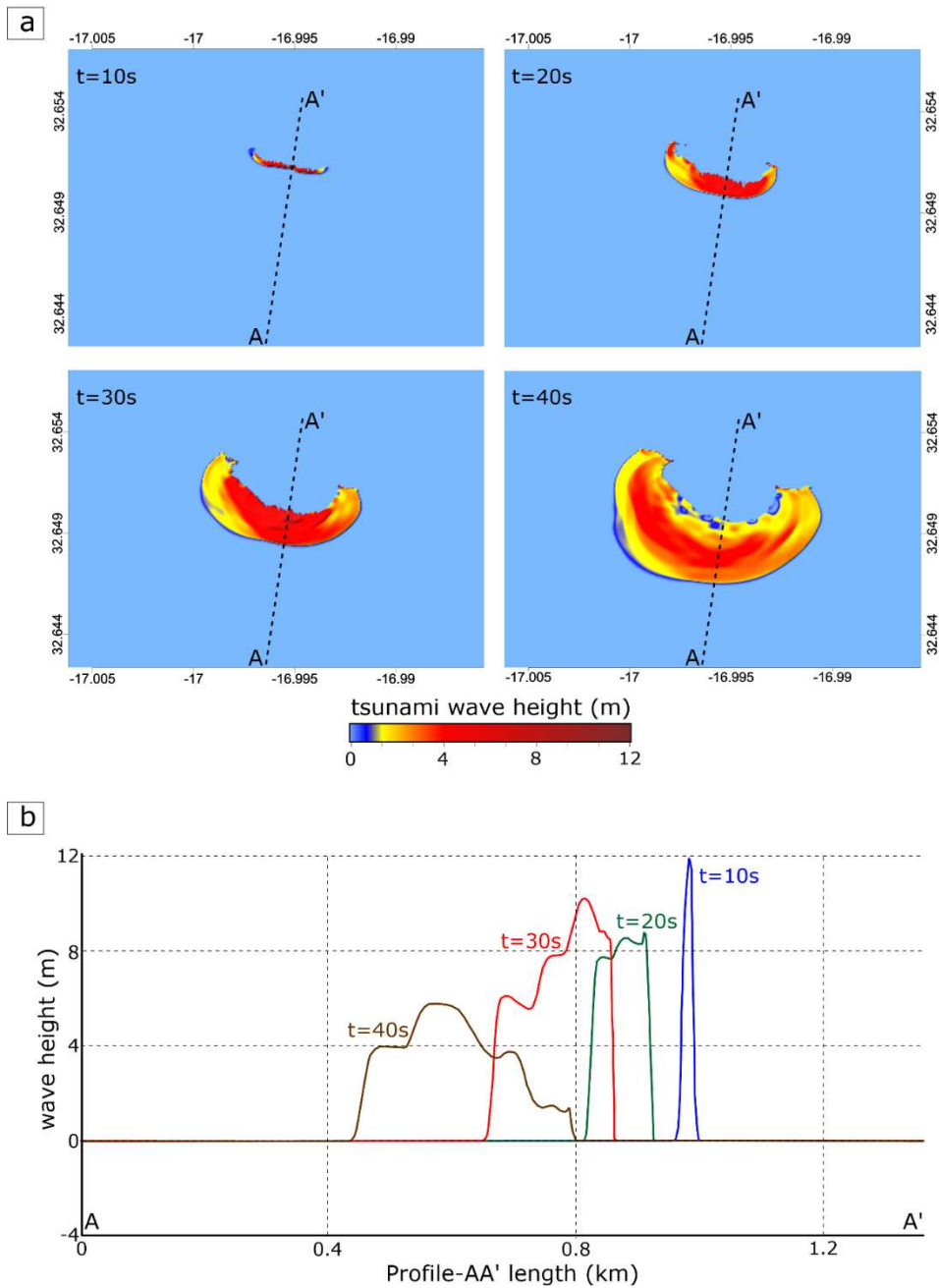


**Fig S3.1:** Wave characteristics of the tsunami generation following the 1930 Cabo Girão cliff-failure. **a)** snapshots of the tsunami generation at 10s, 20s, 30s and 40s (the time the landslide reaches the steady state), AA' is the profile where the waveforms are extracted; **b)** evolution of the tsunami wave generation along the AA' profile, showing the formation of a solitary-type wave with a wavelength less than 0.4 km.

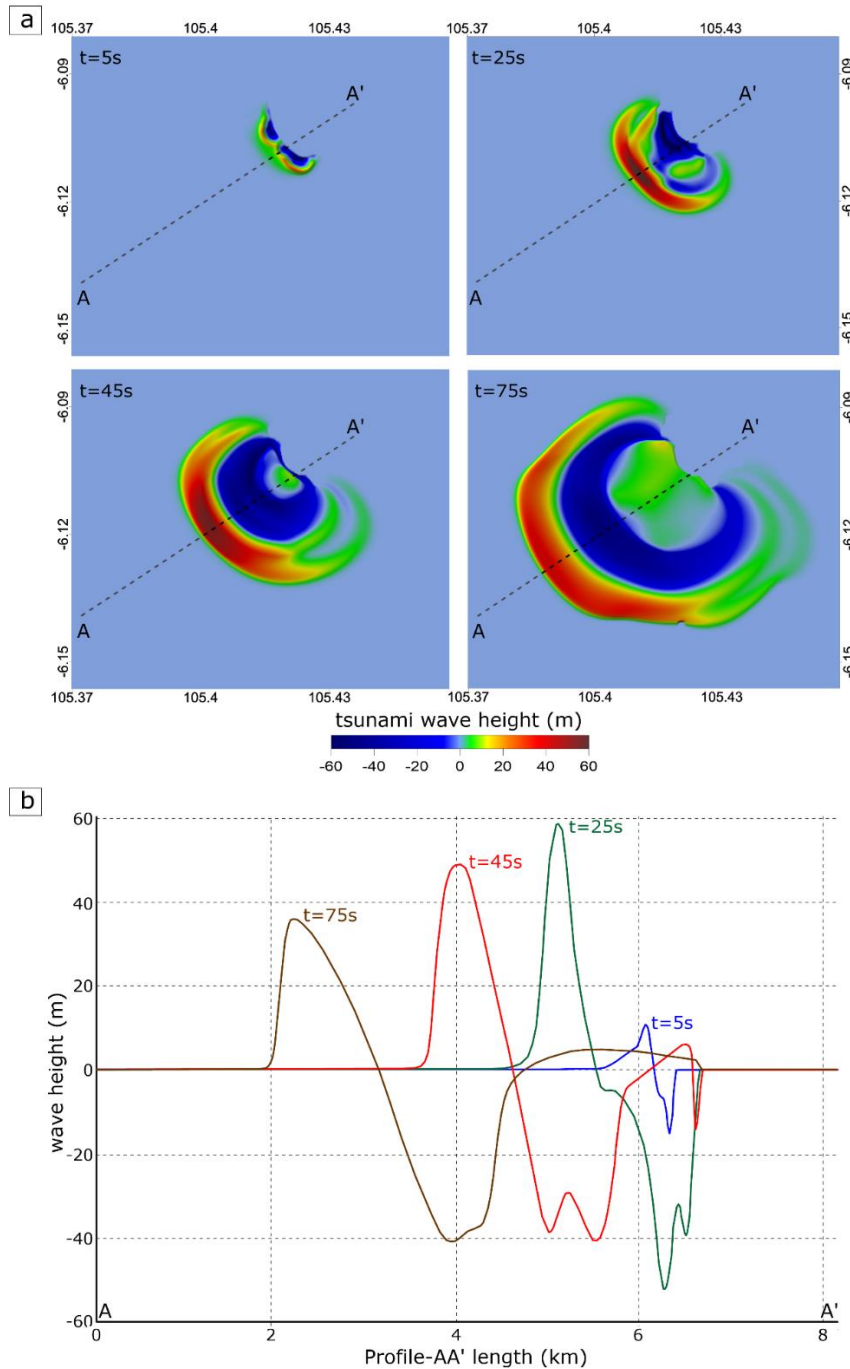


**Fig S3.2:** Wave characteristics of the tsunami generation following the 2018 Anak Krakatau flank-collapse (landslide volume  $0.135 \text{ km}^3$ , see Omira and Ramalho, 2020). **a)** snapshots of the tsunami generation at 5s, 25s, 45s and 75s (the time the landslide reaches the steady state), AA' is the profile where the waveforms are extracted; **b)** evolution of the tsunami wave generation along the AA' profile, showing the formation of an N-wave wave with a large depression and a wavelength of about 3 km.